The Astrophysical Journal, 877:59 (21pp), 2019 May 20 https://doi.org/10.3847/1538-4357/ab12e2

Quiet-Sun Explosive Events Observed in He II λ304 with *MOSES-06*

Thomas Rust and Charles C. Kankelborg
Physics Department, Montana State University, P.O. Box 173840, Bozeman, MT 59717-3840, USA; thomas.rust1@montana.edu
Received 2018 December 7; revised 2019 March 13; accepted 2019 March 22; published 2019 May 24

Abstract

In this paper the unique data from the *Multi-Order Solar Extreme-Ultraviolet Spectrograph* (*MOSES*) are used to investigate transition region explosive events in the He II λ304 spectral line. Particular attention is paid to two example events: one blueshifted jet and one bidirectional jet. Observations suggest that these events consist exclusively of high-velocity ($\sim$100 km s^{-1}) plasma. These two and other examples presented here exhibit a striking lack of emission in the line core. No acceleration phase is observed at the onset of either event. In total, 41 examples of explosive events are identified, including 5 blueshifted jets, 2 redshifted jets, and 10 bidirectional jets. The remaining 24 events resist simple classification, but observations indicate compact, highly Doppler-shifted emission. Event spatial scales and lifetimes are consistent with published explosive event characteristics. Data from the Michelson Doppler Imager provide magnetic context to the *MOSES* observations. Bidirectional jets lacking line core emission are interesting because they are predicted in models of Petschek reconnection in the transition region.

Key words: instrumentation: spectrographs – magnetic reconnection – Sun: transition region – Sun: UV radiation – techniques: imaging spectroscopy

Supporting material: animations

1. Introduction

1.1. Transition Region Explosive Events

Transition region explosive event is the name given by Dere et al. (1984) to describe slit spectrograph observations of enhanced emission in the far (supersonic) wings of transition region spectral line profiles. They were first reported by Brueckner & Bartoe (1983) and were characterized as jets or turbulent events depending on whether enhanced emission was present in one or both line wings.

Explosive events have been observed in many transition region spectral lines. These include C II λ1334/λ1336 (2×10^4 K), Si IV λ1403 (8×10^4 K), C IV λ1548 (1×10^5 K), N V λ1239 (2×10^5 K; Brueckner & Bartoe 1983), and He II λ304 (8×10^4 K; Fox et al. 2010). The Si IV λ1393/λ1402 (8×10^4 K) line pair has been a popular choice for explosive event studies (Innes et al. 1997, 2015; Innes 2001; Ning et al. 2004). The average properties of explosive events observed in C IV from Dere et al. (1989) are summarized in Table 1. Explosive events have been observed with several instruments, including the High Resolution Telescope and Spectrograph (Brueckner & Bartoe 1983; Porter & Dere 1991), the Solar Ultraviolet Measurements of Emitted Radiation (Wilhelm et al. 1995; Innes et al. 1997) instrument aboard the *Solar and Heliospheric Observatory* (*SOHO*), the *Multi-Order Solar EUV Spectrograph* (*MOSES*; Fox et al. 2010), and the *Interface Region Imaging Spectrograph* (*IRIS*; DePontieu et al. 2014; Innes et al. 2015).

Explosive events are typically located above weak mixed-polarity fields along the edges of the quiet-Sun magnetic network (Porter & Dere 1991) and are associated with photospheric flux emergence (Dere et al. 1991) and cancellation (Chae et al. 1998). Due to the correlation between explosive event locations and the magnetic network, Dere et al. (1991) first suggested that explosive events are driven by magnetic reconnection (Priest & Forbes 2007) and that the rate of energy release, based on explosive event lifetimes, is consistent with the fast reconnection model of Petschek (1964).

Explosive events sometimes show a spatial offset between red and blue wings (Dere et al. 1989) and between the wings and the core emission (Ning et al. 2004). Innes et al. (1997) reported spatially offset wings that moved outward from a fixed location over time; they interpreted these results as bidirectional flows resulting from magnetic reconnection in the transition region. Explosive events often show no detectable sky plane motion (Dere et al. 1989).

Many studies have looked at whether energy release in explosive events contributes significant mass and energy to the solar wind and coronal heating, respectively. The energy required to heat the corona is approximately 3×10^5 erg cm^{-2} s^{-1} (Withbroe & Noyes 1977). The global energy requirement is therefore 2×10^{28} erg s^{-1}. Assuming the birth rates and energies associated with explosive events (Table 1), it seems unlikely that explosive events contribute significantly to the coronal energy budget. Dere et al. (1989) and Teriaca et al. (2004) concluded that explosive events do not contribute significantly to coronal heating. On the other hand, it has been argued that explosive events may contribute significantly to the coronal energy budget as part of a range of small-scale energetic events, some currently undetectable (Winebarger et al. 2002). It has been estimated that explosive events may contribute significant mass to the solar wind (Brueckner & Bartoe 1983; Dere et al. 1989).

1.2. Explosive Event Magnetic Reconnection Models

Explosive events are interesting in part because they may be observational signatures of magnetic reconnection in the transition region. Magnetic reconnection is a fundamental plasma process in which magnetic energy is converted to plasma kinetic energy. Reconnection is most often associated

Table 1
Properties of C IV (10^5 K) Explosive Events from Dere et al. (1989)

Parameter	Value
Peak spectroscopic velocity	110 km s^{-1}
Spatial scale	1600 km (2″)
Lifetimes	60 s
QS birth rate	1×10^{-20} cm^{-2} s^{-1}
CH birth rate	4×10^{-21} cm^{-2} s^{-1}
Mass	6×10^{8} g
Kinetic energy	6×10^{22} erg

Note. QS stands for quiet Sun, and CH stands for coronal hole.

with energy release in the corona observed as solar flares. Energy release in reconnection events varies by orders of magnitude from 10^{24} erg in nanoflares (Parker 1988) to 10^{28}–10^{32} erg in medium to large flares (Cargill 2013). Magnetic reconnection is ubiquitous in the solar atmosphere yet is still poorly understood. This is due in part to low emission measure in the expected (coronal) reconnection sites, and the observations are necessarily indirect (Savage et al. 2012). Emission measure in denser transition region plasmas should be two orders of magnitude greater than that in the corona, which suggests that it may be possible to directly observe reconnection sites.

The fast directional and bidirectional flows suggested by spectroscopic measurements of transition region explosive events may be due to plasma that is accelerated as magnetic field lines reconnect and retract to a new lower-energy configuration (Innes et al. 1997). The Doppler speeds observed in explosive events are reasonable values for the Alfvén speed in the transition region (Dere et al. 1991). The Alfvén speed is the predicted outflow speed in magnetic reconnection (Priest & Forbes 2007). If the reconnection scenario is correct, then explosive event observations provide powerful diagnostics of the reconnection process itself. Specific reconnection models to date have difficulty explaining all of the observed features of all explosive events.

Innes & Tóth (1999) modeled Petschek reconnection in the context of transition region explosive events. Their results show that at intermediate transition region temperatures (8×10^4–2×10^5 K) the expected line profiles show almost no emission from low-velocity plasma and consist entirely of emission from fast, oppositely directed jets. Importantly, there is no line core emission in this model.

On the other hand, line core brightening associated with explosive events has frequently been reported (Dere et al. 1991; Innes et al. 1997; Innes 2001). Ning et al. (2004) reported a spatial separation between the core and wing emission. Innes et al. (2015) showed examples of line core brightening in explosive events observed in Si IV λ1402 with *IRIS*. In order to explain the presence of this low-velocity emission, Innes et al. (2015) modeled reconnection in a scenario where the tearing mode instability (Priest & Forbes 2007) results in the creation of magnetic islands. The plasma in these islands is confined and explains the line core emission.

The time evolution of the line profiles from the plasmoid model of Innes et al. (2015) can be described in three separate phases. First, an acceleration phase lasting 60 s shows plasma being accelerated from rest into bidirectional jets at the characteristic Alfvén speed. The next phase lasts approximately 150 s and is similar to the steady-state Petschek model of Innes & Tóth (1999): wing emission at the Alfvén speed and no emission from low-velocity plasma, i.e., no line core. Core brightening begins after 300 s, with core emission dominating the profiles through the end of the simulation (400 s).

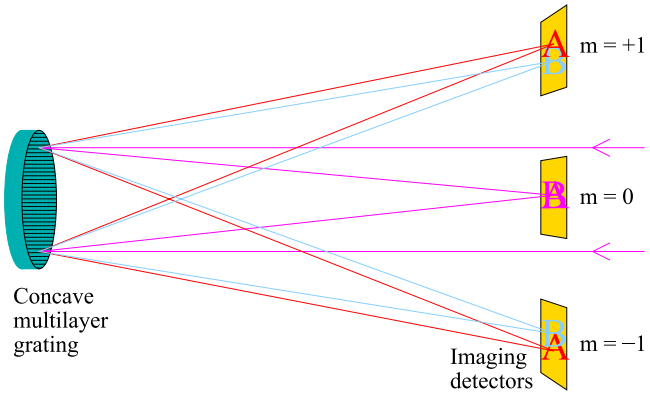

Figure 1. Conceptual model of the *MOSES* instrument. Wide-field images are recorded at multiple orders of a concave diffraction grating. Recovery of spectra from the data generally requires tomographic inversion. A narrowband multilayer coating limits the information content of the data to keep the inversion tractable.

It is expected that the detailed reconnection process will vary with different physical conditions. This expectation has been described by a reconnection phase diagram (Ji & Daughton 2011). If explosive events are due to reconnection in the transition region, it may be that the observed variability in the line profiles is due to different kinds of reconnection. Given that explosive events occur rather frequently, there is great potential to study reconnection itself under transition region conditions. The particular reconnection models of Innes & Tóth (1999) and Innes et al. (2015) suggest that the observed strength of emission in the line core is a vital clue to help distinguish which reconnection process is at work.

1.3. MOSES-06

MOSES (Kankelborg & Thomas 2001) is a slitless imaging spectrograph designed to measure co-temporal spectra over a wide field of view. *MOSES* forms wide-field solar images in three spectral orders of a concave diffraction grating. These spectral orders will be labeled $m = -1$, $m = 0$, and $m = 1$. The images formed in these spectral orders will be called $\mathcal{I}_{-1}$, $\mathcal{I}_0$, and $\mathcal{I}_{+1}$, respectively. The $\mathcal{I}_0$ image is not dispersed and unambiguously shows the spatial distribution of emission. For the $\mathcal{I}_{-1}$ and $\mathcal{I}_{+1}$ images, formed in the dispersed ($m = -1$ and $m = +1$) spectral orders, the image intensity distribution depends not only on the location but also on the spectrum of the emission. Emission at wavelengths to the red or blue of the spectrograph rest wavelength is observed to be spatially shifted along the dispersion direction relative to the $\mathcal{I}_0$ image. A conceptual model of the *MOSES* instrument is shown in Figure 1.

MOSES is a rocket-borne instrument that has flown twice, once in 2006 and again in 2015. This paper concerns the observations from the first flight, *MOSES-06* (Fox et al. 2010; Fox 2011), which flew on 2006 February 8 and was designed to observe the lower transition region He II λ304 spectral line (Section 1.4). The optical characteristics of the *MOSES-06* instrument are shown in Table 2.

The distribution of intensity in the mth-order *MOSES-06* image may be modeled as

$$\mathcal{I}_m(x, y) \propto \{\mathcal{I}^0_m \ * \ \mathcal{P}_m\}(x, y) + n(x, y). \quad (1)$$

In Equation (1) $\mathcal{P}_m(x, y)$ is the point-spread function in the mth order, $n(x, y)$ is additive noise, and $\mathcal{I}^0_m$ is the mth-order ideal geometrical optics image given by Kankelborg & Thomas (2001) and Fox (2011) as

$$\mathcal{I}^0_m(x, y) \propto \int_\lambda B(\lambda)\nu(x - m\lambda, y, \lambda)d\lambda. \quad (2)$$

In Equation (2) $\nu(x, y, \lambda)$ is the line-of-sight-integrated solar spectral radiance, $B(\lambda)$ is the instrument passband, and x, y are image pixel coordinates. Here λ is defined as the change in wavelength relative to the rest wavelength (303.8 Å) and is measured in instrument pixels. The conversion from wavelength to pixel units (29 m Å pixel^{-1}; Table 2) is an expression of the instrument dispersion.

Equation (2) says that the *MOSES* images are *projections* of the solar spectral radiance. In general, it is necessary to perform a tomographic inversion (e.g., Kak & Slaney 1988; Fox 2011) to recover spectra from the *MOSES* data. Ambiguity in the data inversion is reduced by limiting the passband B of the instrument. *MOSES* employs narrowband multilayer coatings to restrict the passband to, ideally, a single spectral line. $\mathcal{I}_0$ is then a narrowband filtergram. In the ideal case all disparities between the dispersed images ($\mathcal{I}_{-1}$ and $\mathcal{I}_{+1}$) and the filtergram ($\mathcal{I}_0$) are attributable to Doppler shifts of the spectral line under study.

1.3.1. MOSES *and Point-like Objects*

Explosive events can present a simpler special case for *MOSES* data analysis because they are *compact*, high-contrast objects possessing high spectroscopic velocities. The effect of limited spatial extent of the emission is similar to the effect of limited field of view imposed by a spectrograph slit. Consider the idealized case of an isolated point object: the measured intensity distribution in the dispersed images will be proportional to the line profile of the emission. It is therefore possible to characterize many explosive events without a full tomographic treatment.

To see this, consider a profile along the dispersion axis of the ideal *MOSES-06* image given the limiting case of a point distribution of spectral radiance, i.e., $\nu(x, y, \lambda) = \nu_0(x, y, \lambda)\delta(x - x_0, y - y_0)$. The $\mathcal{I}_m{}^0$ may be calculated from Equation (2):[1]

$$\mathcal{I}^0_m(x, y) \propto \int_\lambda \nu_0(x - m\lambda, y, \lambda)\delta(x - x_0 - m\lambda, y - y_0)d\lambda. \quad (3)$$

Taking the integral, the resulting profiles in the mth spectral order image ($m \neq 0$) are given by

$$\mathcal{I}^0_m(x, y = y_0) \propto \nu_0(x_0, y_0, m^{-1}(x - x_0)). \quad (4)$$

In words, the $\mathcal{I}_{-1}$ and $\mathcal{I}_{+1}$ dispersion direction *spatial* profiles through an isolated point source are proportional to the *spectral* line profile of the point source. They are also redundant, mirrored about the coordinate $x = x_0$. In general, the profiles will be a function of wavelength λ (evaluation of λ in pixel coordinates is an expression of the spectrograph dispersion, as discussed in Section 1.3). Further, as noted in the previous section, if the radiance arises only from the target spectral line, here specifically He II λ304, then in the ideal image case disparities between the profiles of the $\mathcal{I}_m$ must be due to Doppler shifts. In this special case the $\mathcal{I}_{-1}$ and $\mathcal{I}_{+1}$ profiles are mirror images of the line profile of the source and may be equivalently considered to be a function of wavelength *or* Doppler velocity. The rest wavelength coordinate, or equivalently the zero Doppler velocity coordinate, is set by the x coordinate of the point source in the $\mathcal{I}_0$ (filtergram) profile. The *MOSES-06* pixels subtend 29 m Å or 29 km s^{-1} (Table 2). It is estimated (Fox 2011, and references therein) that the He II λ304 line accounts for 95% of photons detected by *MOSES-06*.

[1] The bandpass $B(\lambda)$ is broad compared to a spectral line and may be considered constant and therefore suppressed in this example.

Table 2
Spectrograph Specifications for the *MOSES-06* Flight

Focal length	4.74 m
Aperture	8 cm square (f/59)
Detectors	Rear Illuminated CCD
Sampling	2048 × 1024 pixels, 13.5 μm pitch
Pixel scale	0.″59, 29 m Å, 29 km s^{-1}, 440 km
FOV	20′ × 10′
Grating	9.48 m sphere, 950 lines mm^{-1}
Coatings	B_4C/Mg_2Si multilayer
Bandpass	20 Å FWHM centered at 307 Å (Owens et al. 2005)
Target line	He II λ303.8

Being compact, explosive event observations are also prone to suffer from resolution effects. In particular, any compact object whose image plane spatial extent is less than that of the image point-spread function will take on the shape of the point-spread function (Equation (1)). Rust (2017, Appendix D) showed many examples of subresolution compact objects in the *MOSES-06* data and derived estimates for the instrument point-spread functions that differ in each spectral order. The point-spread functions have a significant impact on the appearance of the data at small resolution scales. In order to properly interpret the *MOSES-06* data at small scales, the point-spread functions must be taken into account. In the case of the profile analysis discussed in this section, this really is no different from resolution issues encountered in slit spectroscopy.

1.4. The He II λ304 Line

The He II λ304 emission line ($\lambda = 303.78$ Å) is the Lyα transition of singly ionized helium. The peak line formation temperature of approximately 80,000 K (MacPherson & Jordan 1999) places the emission in the lower transition region. The thermal speed $v_T = \sqrt{k_B T/m_{\rm He}}$ at this temperature is approximately 13 km s^{-1}. Andretta et al. (2000) reported that the average He II λ304 spectral line profile was very nearly Gaussian in both the quiet and active Sun. The λ304 line is one of the brightest of the transition region EUV lines (e.g., Tousey et al. 1973). The λ304 line has an anomalous intensity with enhancement of up to an order of magnitude relative to model predictions that reproduce the intensities of other transition region lines (Jordan 1975; MacPherson & Jordan 1999).

1.5. Paper Outline

The paper is organized as follows. Section 2 describes the *MOSES-06* data set along with coronal and magnetic context

data from *SOHO*. Section 3 describes data reduction and presents examples of the *MOSES-06* and context images. In Section 4 difference images are used to locate spectrally interesting features in the data. Of particular interest are compact regions whose properties are consistent with the explosive event properties described in Section 1.1. In Section 5 two explosive event observations are presented in detail. The filtergram images of these events show a compact object brighten with respect to the surrounding emission. The *MOSES-06* dispersed images reveal the spectral character of these events. One event is strongly blueshifted. The other has two components, one strongly redshifted and one strongly blueshifted. These events are identified as a blueshifted jet and a bidirectional jet, respectively. The Doppler shift magnitudes are approximately 100 km s^{-1}, consistent with other reported explosive event velocities. Both events appear to have little or no emission from low-velocity plasma. Both events exhibit a "switch-on" characteristic with no acceleration phase observed during the event onset despite a 10 s cadence. This section also describes the magnetic context of these example events, and estimates for mass and energy are derived. Section 6 presents additional examples of explosive events in the *MOSES-06* data. Explosive events do not appear to be rare in He II λ304.

2. Data

MOSES-06 flew on 2006 February 8 at 18:44:01 UT aboard a Terrier-boosted Black Brant sounding rocket from White Sands Missile Range in New Mexico, USA. The optical characteristics of the *MOSES-06* instrument are shown in Table 2. In all *MOSES-06* spent approximately 5 minutes above 160 km and recorded 27 data exposures between 18:44:17 and 18:49:13 UT. Each exposure consists of the three images $\mathcal{I}_{-1}$, $\mathcal{I}_0$, and $\mathcal{I}_{+1}$, where the subscript indicates the spectral order. The images are 2048 × 1024 pixels with angular sampling rate of 0.″59 pixel^{-1}. Dark exposures were recorded during flight before and after the data sequence to measure the detector pedestal. The raw images are pedestal subtracted and then corrected for flat-field variation. The flat fields were measured by Fox (2011).

The times, exposure lengths, and altitudes of the data are shown in Table 3. Exposure times vary between 0.25 and 24 s, with approximately 6 s readout time in between. The long exposures are saturated in the brightest regions. The shortest exposures are somewhat underexposed. Fifteen exposures taken midflight between 18:47:15 UT and 18:49:24.75 UT at nearly uniform 9 s cadence (exposure + readout) are almost perfectly exposed.

Co-observations made by the instrument suite aboard *SOHO* provide context for the *MOSES-06* observations. The Extreme-ultraviolet Imaging Telescope (EIT) (Delaboudinière et al. 1995) is a normal incidence multilayer EUV filtergraph. EIT measures full-disk images in passbands dominated by He II λ304, Fe IX–X λ171, Fe XII λ195, and Fe XV λ284. The temperatures of formation of these lines are 8.0×10^4 K, 1.3×10^6 K, 1.6×10^6 K, and 2.0×10^6 K, respectively. The Michelson Doppler Imager (MDI; Scherrer et al. 1995) aboard *SOHO* measures line-of-sight photospheric magnetograms. An MDI magnetogram taken on 2006 February 8 at 20:48:27 UT, 2 hr after the *MOSES-06* flight, will be used to provide magnetic context to the EUV observations.

Table 3
Catalog of *MOSES-06* Data Exposures (from Fox 2011)

Exposure # (n)	Start (UT)	End (UT)	Duration (s)	Altitude (km)
0	18:45:54.00	18:45:54.25	0.25000	161.80–162.14
1	18:46:00.30	18:46:01.05	0.75000	170.32–171.30
2	18:46:07.00	18:46:08.50	1.50000	178.84–180.69
3	18:46:14.55	18:46:20.55	6.00000	187.87–194.73
4	18:46:26.70	18:46:38.70	12.0000	201.46–213.49
5	18:46:44.95	18:47:08.99	24.0396	219.19–237.97
6	18:47:15.15	18:47:18.22	3.06981	241.99–243.84
7	18:47:24.40	18:47:27.48	3.07972	247.26–248.85
8	18:47:33.65	18:47:36.75	3.09981	251.76–253.11
9	18:47:42.95	18:47:46.03	3.07982	255.53–256.61
10	18:47:52.20	18:47:55.27	3.06970	258.52–259.34
11	18:48:01.45	18:48:04.45	3.00000	260.71–261.26
12	18:48:10.70	18:48:13.77	3.06974	262.14–262.44
13	18:48:19.95	18:48:23.04	3.08979	262.79–262.84
14	18:48:29.20	18:48:32.28	3.07981	262.67–262.46
15	18:48:38.60	18:48:41.60	3.00000	261.76–261.30
16	18:48:47.85	18:48:50.85	3.00000	260.07–259.35
17	18:48:57.05	18:49:00.14	3.08983	257.65–256.66
18	18:49:06.30	18:49:09.36	3.05984	254.42–253.18
19	18:49:15.50	18:49:18.58	3.07980	250.44–248.94
20	18:49:24.75	18:49:27.84	3.08983	245.70–243.94
21	18:49:34.10	18:49:58.19	24.0897	240.06–221.94
22	18:50:04.35	18:50:16.35	12.0000	216.50–204.83
23	18:50:22.65	18:50:28.65	6.00000	198.06–191.37
24	18:50:35.00	18:50:36.56	1.55980	183.99–182.11
25	18:50:42.75	18:50:43.50	0.75000	174.35–173.39
26	18:50:49.70	18:50:49.95	0.25000	165.34–165.01

3. Data Reduction

The dark-subtracted, flat-field-corrected data must be aligned and normalized prior to quantitative analysis. These data reduction steps are briefly described in this section.

3.1. Co-alignment

3.1.1. MOSES *Images*

Estimation of Doppler shifts from the *MOSES-06* data is sensitive to the spatial co-alignment between the three images ($\mathcal{I}_{-1}$, $\mathcal{I}_0$, and $\mathcal{I}_{+1}$) measured in a given exposure. Given the instrument dispersion (29 km s^{-1} pixel^{-1}), it is desirable to achieve subpixel co-alignment. The co-alignment method used in this paper is that of Fox et al. (2010). In this method it is assumed that the mapping of coordinates from $\mathcal{I}_{-1}$ to $\mathcal{I}_0$ and from $\mathcal{I}_{+1}$ to $\mathcal{I}_0$ is described by a linear polynomial transformation. The polynomial coefficients are optimized with respect to the reduced χ^2 statistic. Fox et al. (2010) report co-alignment repeatability from exposure to exposure of <0.2 pixel rms. This co-alignment assumes that there is zero net Doppler shift averaged over the field of view.

3.1.2. MOSES *to* SOHO-*EIT* λ*304*

Solar coordinates are obtained from co-alignment of the $\mathcal{I}_0$ with a *SOHO*-EIT λ304 image via cross correlation. The EIT image was taken at 18:39:34 UT, about 9 minutes prior to the midpoint of the *MOSES-06* flight. The *MOSES-06* images are oriented with east–west along the horizontal (x) axis and south–north along the vertical (y) axis, with solar west in the $+x$-direction and solar north in the $+y$-direction. The

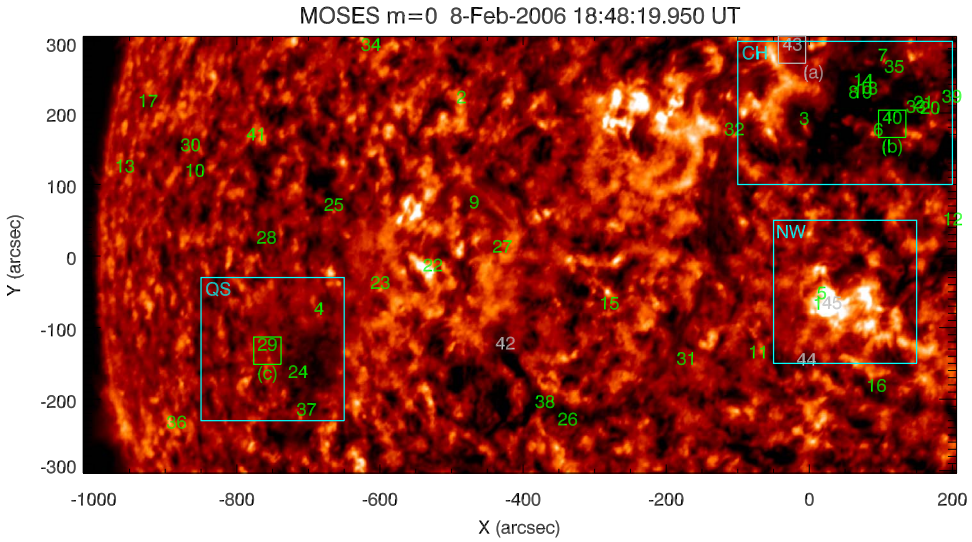

Figure 2. $\mathcal{I}_0$, exposure number $n = 13$, following data reduction and co-alignment. For display the image has been logarithmically scaled after clipping the brightest and darkest 0.3% of all pixels. The three large boxed regions of interest enclose strong network emission (NW), quiet Sun (QS), and a coronal hole (CH). The three small boxed regions of interest labeled (a), (b), and (c) indicate the fields of view for the compact object observations presented in Section 5. The green numbers 1–41 indicate the positions of explosive events. The gray numbers 42–45 show the locations of compact objects that are not explosive events.

instrument field of view is approximately $x \in [-1004'', 197'']$ by $y \in [-302'', 299'']$ heliocentric Cartesian coordinates. The dispersion direction is along the x-axis. Emission to the blue of He II λ304 line center shifts toward $+x$ (west) in $\mathcal{I}_{+1}$ and $-x$ (east) in $\mathcal{I}_{-1}$ relative to $\mathcal{I}_0$; emission to the red of He II λ304 is shifted in the opposite sense.

3.2. Normalization

Three *MOSES-06* channels are normalized for source intensity to account for atmospheric extinction and channel sensitivity.

Figure 2 shows an example exposure of the prepared $\mathcal{I}_0$. The image is a high-quality filtergram with very good contrast and resolution. Solar activity was very low on this date, and the mottled emission of the quiet-Sun network dominates over most of the field of view. The primary exception is a coronal hole in the upper NW corner, between approximately $x \in [0'', 200'']$ and $y \in [100'', 300'']$. A dark filament channel runs in a backward "j" shape starting at coordinates $[-100'', 200'']$, reaching a low point at $[-300'', -200'']$, then curling upward to terminate at about $[-450'', -100'']$. No active regions were present on this date. Three regions, centered on coordinates $[-550'', 0'']$, $[-250'', 200'']$, and $[50'', -75'']$, show enhanced emission relative to the surrounding network.

Examples of $\mathcal{I}_{-1}$ and $\mathcal{I}_{+1}$, along with context data from *SOHO*, are shown in Figure 3. At a glance the $\mathcal{I}_{-1}$ and $\mathcal{I}_{+1}$ appear very similar to $\mathcal{I}_0$. Beginning in Section 4, the differences between the $\mathcal{I}_m$ will be demonstrated and interpreted. The *SOHO* context data consist of nearly co-temporal EIT 304, 171, and 284 Å images and an MDI line-of-sight photospheric magnetogram. The *SOHO* data have been cropped to the *MOSES-06* field of view. The magnetogram was made on 2006 February 8 at 20:48:27 UT, 2 hr after the *MOSES-06* flight. In order to facilitate comparison with the *MOSES-06* measurements, the magnetogram has been derotated by 2 hr using the *drot_map*() function, written in the Interactive Data Language and part of the SolarSoft software suite (Freeland & Handy 1998). The time shown in the figure is the derotated time. Bright concentrations in the magnetogram constitute the magnetic network field that has been concentrated by convective motions into the downflow lanes bordering supergranular cells. The strongest magnetic regions underlie the brightest emission in the *MOSES-06* data (Figure 2 and top row of Figure 3), as well as the loops visible in the coronal data (bottom row of Figure 3). Away from the stronger concentrations the mixed gray scale shows weak, mixed-polarity fields. The EIT 171 and 284 Å images show the coronal context of the *MOSES-06* observations. A coronal hole in the northwest corner of the *MOSES* field of view is particularly visible in the 284 Å channel. The strongest network regions in the *MOSES-06* data lie below bright loop structures visible at these coronal temperatures. Both channels show brightening above the limb.

4. Difference Images

The search for interesting phenomena in the *MOSES-06* data set begins with the difference images $d_{(0,-1)} = \mathcal{I}_0 - \mathcal{I}_{-1}$ and $d_{(0,+1)} = \mathcal{I}_0 - \mathcal{I}_{+1}$. Examples of difference images are shown in Figure 4.

The structure in the difference images is striking. Perhaps the most obvious features have coronal morphology: the limb and the loops seen near $[50'', -75'']$, $[-550'', 100'']$, and $[-350'', 225'']$ (the "wishbone") in EIT coronal images (Figures 3(e) and (f)) are all easily discernible and positive in the difference images. Positive differences (e.g., $\mathcal{I}_0 > \mathcal{I}_{-1}$) are expected at locations where emission away from the rest wavelength (He II λ304) is shifted spatially in the dispersed images ($\mathcal{I}_{-1}$ and $\mathcal{I}_{+1}$). The coronal morphology of these features suggests that this is contaminant emission due to ions at coronal temperatures, not singly ionized helium. These likely contaminant lines, along with wavelength estimates, are discussed further in Rust (2017, chap. 2).

A second class of objects in the difference images are strong, compact, and *isolated* positive features scattered across the field of view. For example, three such objects form a bright triangle (coordinates $[90'', 170'']$, $[100'', 275'']$, and $[170'', 200'']$) in the

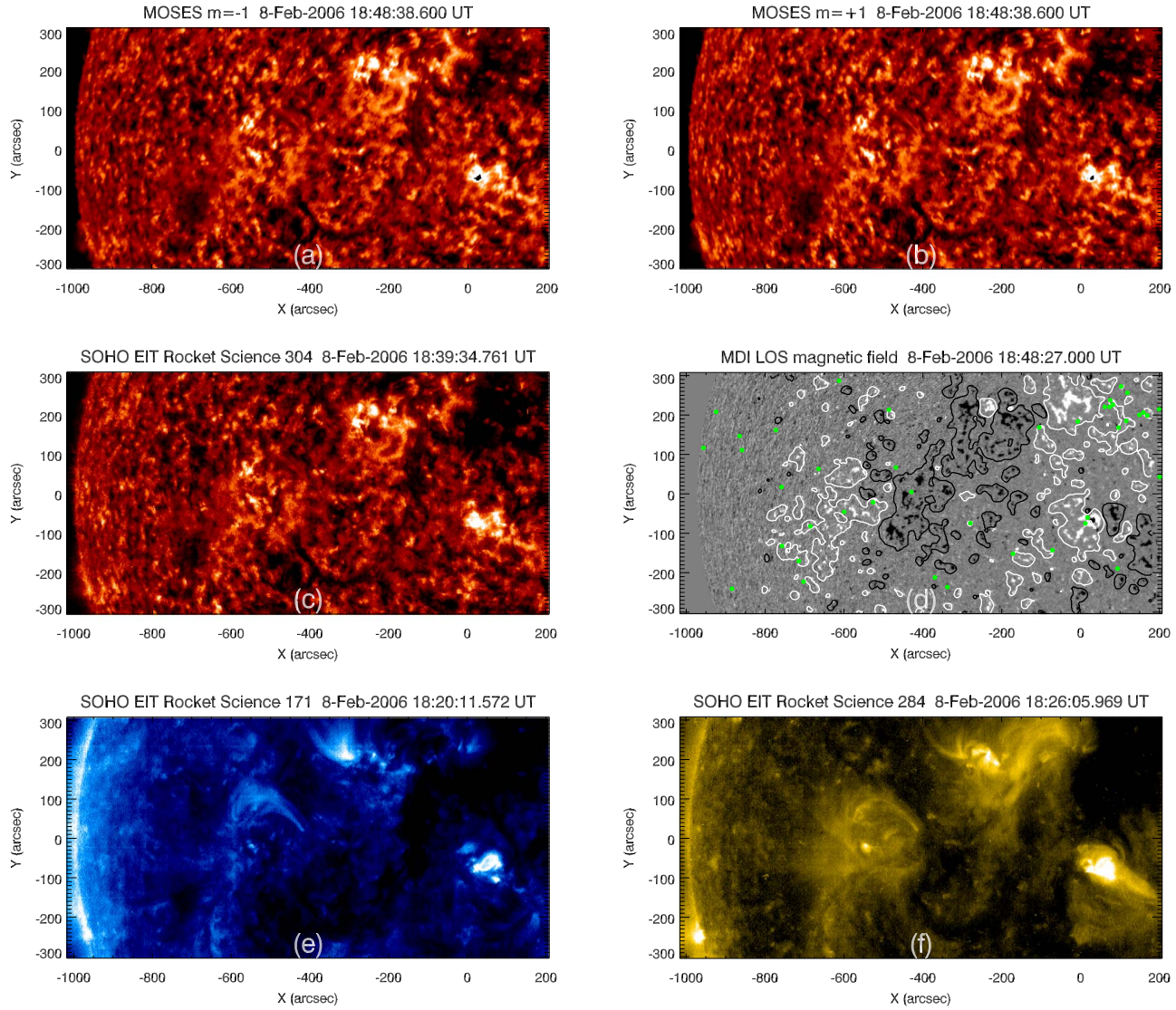

Figure 3. *MOSES-06* dispersed images (top row) and context data from EIT. From left to right, top to bottom: (a) $\mathcal{I}_{-1}$ and (b) $\mathcal{I}_{+1}$, exposure number $n = 13$, following data reduction and co-alignment. The images are logarithmically scaled with the same clipping used for the $\mathcal{I}_0$ image in Figure 2. North is up, west is right, and the spectrograph dispersion is along the E−W axis. The black pixels located in the center of the bright region at about [20″, −75″] are saturated. (c) EIT 304 Å image cropped to the *MOSES-06* field of view. (d) Line-of-sight magnetic field measured by MDI. The display is linearly scaled and clipped at about ±80 G. Positive-polarity magnetic elements are white, and negative-polarity elements are black. Gray regions are regions with weak or no magnetic field. The data have been rotated backward in time by 2 hr for comparison with the *MOSES-06* data (see text). The time shown is the derotated time. Overplotted on the magnetic data are +5 g (white) and −5 g (black) contours of a potential field extrapolation. The green points indicate explosive event locations. (e) EIT 171 Å and (f) EIT 284 Å, cropped to the *MOSES-06* field of view. Images are logarithmically scaled with 0.3% clipping.

coronal hole region of $d_{(0,-1)}$. Comparison with $d_{(0,+1)}$ shows corresponding features for two of the three; the SE object shows significantly less contrast in $d_{(0,+1)}$. Another example, strongly positive in both difference images, sits about 50″ east of the eastern tip of the "wishbone."

The small-scale features in the difference images may be isolated for further study through the use of a wavelet transform. In general terms wavelet transforms may be used to view images in a range of *resolution scales*. The à trous algorithm (Holschneider et al. 1990; Shensa 1992) is used to calculate the wavelet transform of the difference images up to scale $j = 2$, the second-finest resolution scale ($j = 1$ is inconveniently noisy).

Figures 5–7 show the small-scale structure of both intensity and difference images within three fields of view covering the coronal hole, a region of quiet Sun, and the strong network, respectively. Clockwise from upper left, Figures 5–7 show (log scaled) $\mathcal{I}_0$, $d_{0,1}$, $\tilde{\mathcal{I}}_0^2$, and $\tilde{d}_{0,-1}^2$, where $\tilde{f}^j$ is the wavelet transform of f at scale j.

Both the intensity images ($\mathcal{I}_0$) and the difference images ($d_{0,-1}$) show significant small-scale variation. The strong differences contoured in Figures 5–7 are almost always associated with significant[2] positive wavelet coefficients. This association can roughly be characterized one of two ways: the strong difference contours can either coincide with the contours of the wavelet coefficients, or the difference contours can lie on the periphery of the positive wavelet coefficients. Notable examples of the former type include the features located at [100″, 270″] and [160″, 200″] in Figure 5 and the feature at

[2] In the present context this term is used subjectively; statistical significance testing is discussed extensively in Rust (2017).

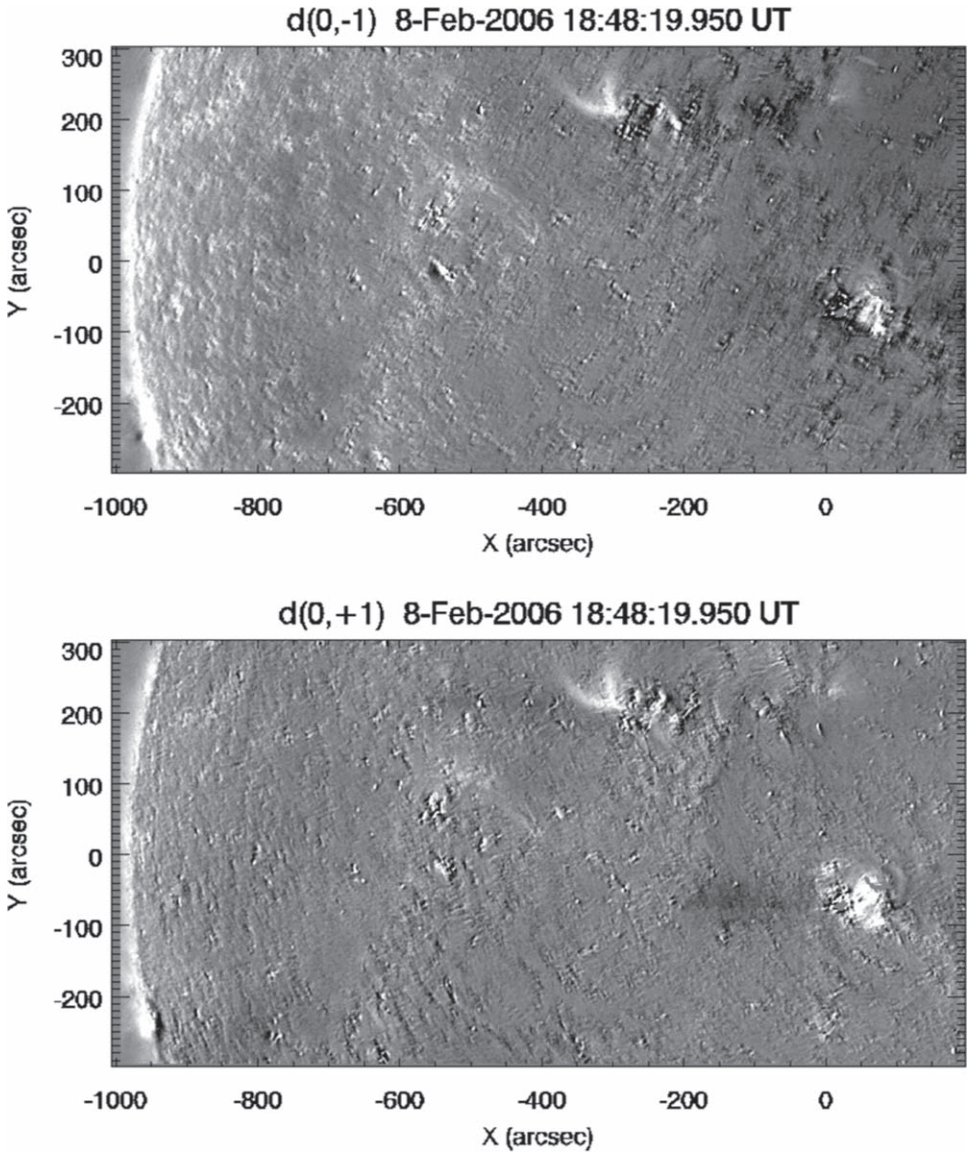

Figure 4. Example difference images $d_{(0,-1)} = \mathcal{I}_0 - \mathcal{I}_{-1}$ (top) and $d_{(0,+1)} = \mathcal{I}_0 - \mathcal{I}_{+1}$ (bottom). Light colors indicate positive differences; dark colors indicate negative differences. The images are displayed on a linear scale and have been clipped at three standard deviations to show faint details.

$[-750'', -130'']$ in Figure 6. These examples are all compact emission with relatively high contrast. They are relatively isolated, i.e., no other strong sources in the immediate neighborhood.

Many of the difference contours are an example of the latter case. Examples are shown in Figure 5 and are indicated with orange arrows. A particular example to be shown in more detail is located at coordinates $[-30'', 285'']$ in Figure 5. Fox (2011) noted that the point-spread functions $\mathcal{P}_m$ differ in each *MOSES-06* spectral order, and those differences manifest themselves as a quadrupolar pattern in difference images. Bright, compact objects show strong signatures in difference images that tend to have the greatest amplitude on the periphery of the actual emission location.

Consider, then, regions with complicated small-scale structure, e.g., the network emission shown in Figure 7. When every compact source produces a quadrupolar pattern in a difference image, it becomes difficult to say whether a particular peak in the difference image is due to Doppler shifts or an artifact caused by the differing point-spread functions. Many strong differences show up in the bright network and across the field of view. What is an artifact, and what is not? In the following section it will be shown by example that at least some of the small-scale disparities seen in $d_{0,-1}$ and $d_{0,+1}$ are due to Doppler-shifted emission from transition region explosive events.

Explosive events are identified first and foremost by their signatures in difference images (Figures 4, 5(b), 6(b), and 7(b)). The classic difference signature of an explosive event in the *MOSES-06* data is a compact region of strong positive difference coupled to adjacent (along the dispersion direction) compact regions of negative difference on one or both sides, depending on whether the emission is blueshifted, redshifted, or both. This difference distribution results as dispersion moves Doppler-shifted photons observed in $\mathcal{I}_{-1}$ and $\mathcal{I}_{+1}$ away from the source location as observed in $\mathcal{I}_0$. Excellent clean examples of this signature are seen in event numbers 7 and 20 in Figure 5, 29 in Figure 6, and 1 in Figure 7. Difference movies, in particular (Figures 5–7 animations), make candidate events

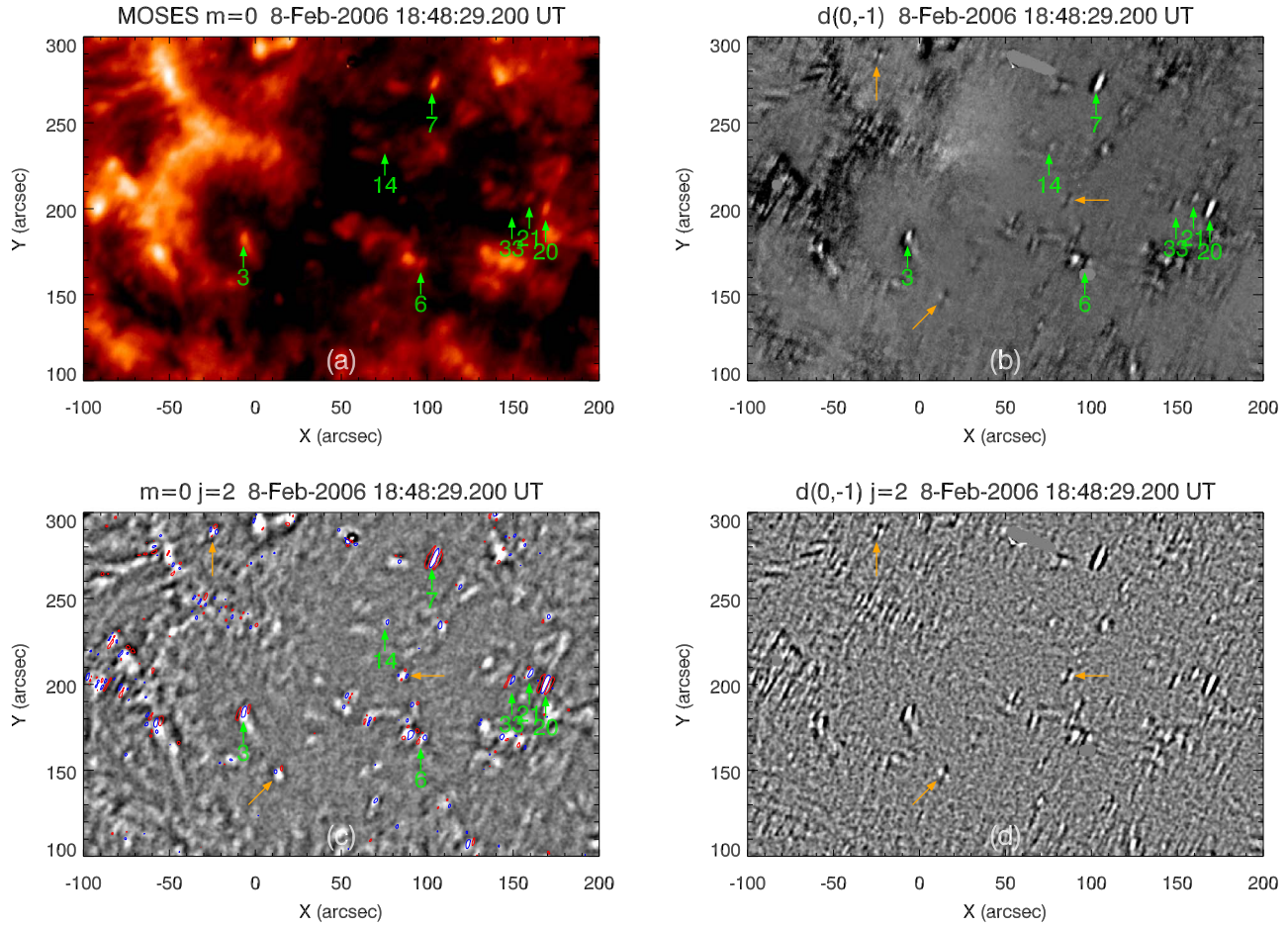

Figure 5. Close-up of the coronal hole (CH box in Figure 2) in the *MOSES-06* data showing the small-scale structure of the region. Panels show (a) log-scaled $\mathcal{I}_0$ intensity, (b) difference image $d_{(0,-1)}$, (c) the $j = 2$ wavelet coefficients $\tilde{\mathcal{I}}^2_z$, and (d) the scale $j = 2$ wavelet coefficients $\tilde{d}^2_{(0,-1)}$. The 3σ contours of $\tilde{d}^2_{(0,-1)}$ are overplotted onto the $\tilde{\mathcal{I}}^2_z$ image. Blue contours are positive differences, and red contours are negative. Numbered arrows point to explosive events identified in this paper that are visible at the time shown in the figure. Compact positive regions in the difference image (panel (b)) indicate likely explosive event locations, as dispersion moves Doppler-shifted photons observed in $\mathcal{I}_{-1}$ and $\mathcal{I}_{+1}$ away from the source location as observed in $\mathcal{I}_0$. Compact bright features in the image data, seen most clearly in the $j = 2$ wavelet coefficients (panel (c)), are also likely locations. At the smallest spatial scales *MOSES-06* is resolution limited and all features take on the shape of the point-spread functions (Rust 2017). When the difference contours roughly coincide with the intensity contours (e.g., 7 and 20 are good examples), the underlying object is usually an explosive event. In other cases, where the difference contours lie on the periphery of the intensity feature (unnumbered orange arrows in panels (b), (c), and (d)), the difference signatures typically arise from disparities in the point-spread functions, which results in the quadrupolar pattern in difference images noted by Fox (2011). An animation of this figure is available in the online journal. The animation shows the full sequence of 27 observations over the ∼5-minute flight. The animation makes it easy to see how explosive event candidates are found in the data as bright compact features in the difference and intensity images that appear to flicker, some transient, others lasting the duration of the flight. Explosive events identified in this paper are labeled with numbered arrows at times when they are clearly visible.

(An animation of this figure is available.)

very clear as the compact strong difference regions scintillate in time.

Compact bright features in the image data, seen most clearly in the $j = 2$ wavelet coefficients (Figures 5(c), 6(c), and 7(c)), are also likely locations, and all known explosive events in the *MOSES-06* data are associated with compact intensity enhancements. At the smallest spatial scales *MOSES-06* is resolution limited and all features take on the shape of the point-spread functions (Rust 2017). Intensity features that most closely resemble the point-spread function in $\mathcal{I}_0$ are particularly good candidates, as the source may then be considered to be an isolated point source (to within our resolution) and the data analysis may be simplified as described in Section 1.3.1.

Explosive events in the *MOSES-06* data most often exhibit both characteristics: strong compact difference signature associated with a compact intensity feature seen in $\mathcal{I}_0$ or the corresponding wavelet data. The nature of the association between the intensity feature and difference signature is a vital clue as to whether the object in question is truly an explosive event. When the difference contours roughly coincide with the $\mathcal{I}_0$ $j = 2$ wavelet intensity contours (e.g., 7 and 20 in Figure 5 are good examples), the underlying object is usually an explosive event. In other cases, where the difference contours lie on the periphery of the intensity feature (unnumbered orange arrows in panels Figures 5(b), (c), and (d)), the difference signatures typically arise from disparities in the point-spread functions.

Thus far automated methods to identify explosive events in the *MOSES-06* data have met with some success but suffer from type I and type II errors. Currently the most reliable identification technique, and that used in this paper, is a hybrid technique. Candidate locations are identified automatically, and in some cases manually, from difference and intensity data. Acceptance of a candidate as an explosive event is made by

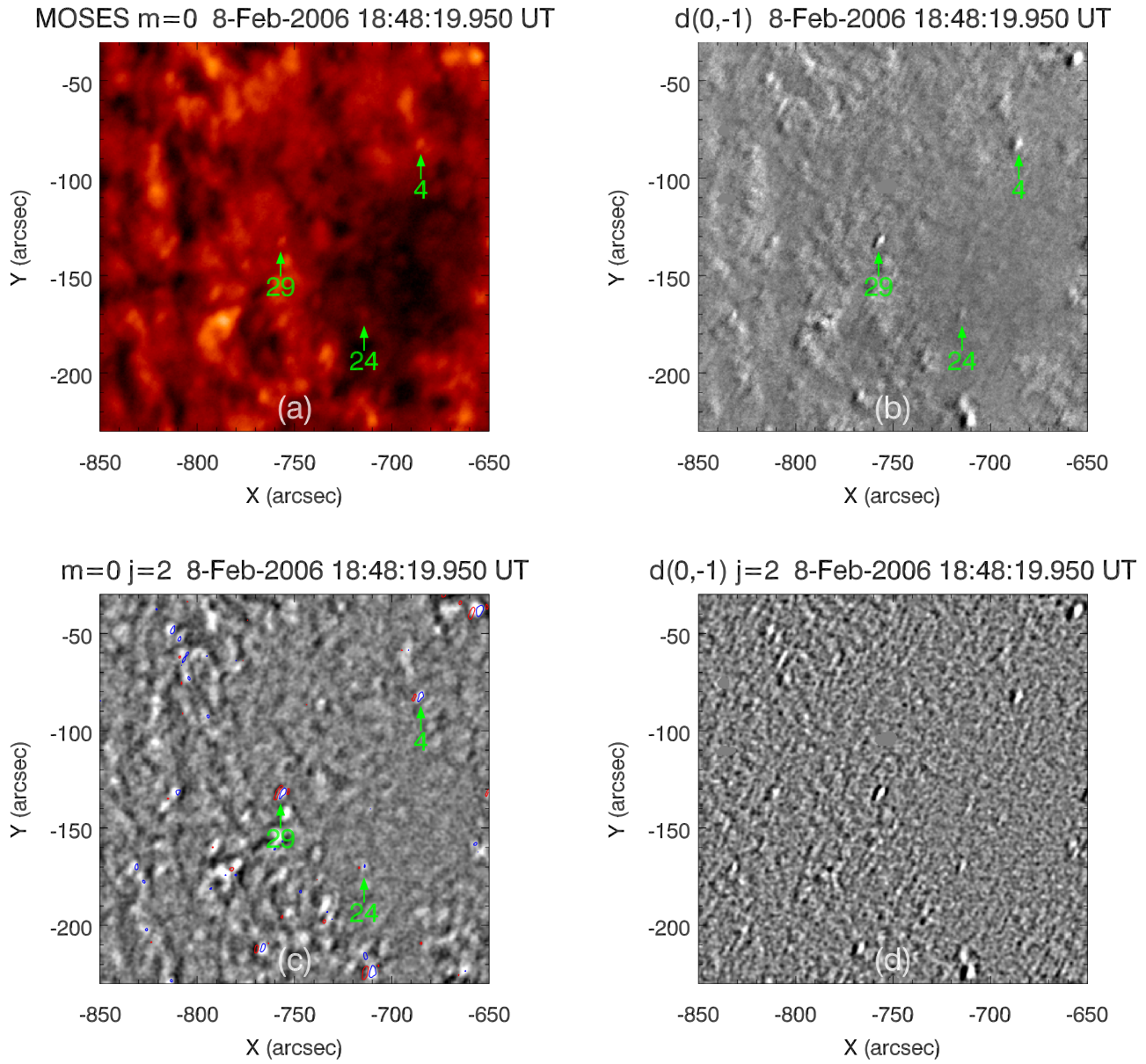

Figure 6. Close-up of a region of quiet Sun (QS box in Figure 2). Panels show (a) log-scaled $\mathcal{I}_0$ intensity, (b) difference image $d_{(0,-1)}$, (c) the $j = 2$ wavelet coefficients $\tilde{\mathcal{I}}_z^2$, and (d) the scale $j = 2$ wavelet coefficients $\tilde{d}_{(0,-1)}^2$. The 3σ contours of $\tilde{d}_{(0,-1)}^2$ are overplotted onto the $\tilde{\mathcal{I}}_z^2$ image. Blue contours are positive differences, and red contours are negative. Numbered arrows point to explosive events identified in this paper that are visible at the time shown in the figure. An animation of this figure is available in the online journal. The animation shows the full sequence of 27 observations over the ~5-minute flight. The animation makes it easy to see how explosive event candidates are found in the data as bright compact features in the difference and intensity images that appear to flicker, some transient, others lasting the duration of the flight. Explosive events identified in this paper are labeled with numbered arrows at times when they are clearly visible.

(An animation of this figure is available.)

manual selection based on watching movies of the events. As will be seen, many of the explosive events are not subtle.

5. Explosive Event Examples

Figure 8 shows three compact sources of emission observed by *MOSES-06*. Each column (labeled (a), (b), and (c)) is a different field of view. Within each column the $\mathcal{I}_{+1}$, $\mathcal{I}_0$, and $\mathcal{I}_{-1}$ channels are ordered from top to bottom, respectively. The objects of interest, compact emission sources, lie in the centers of the fields of view. Recall that the $\mathcal{I}_0$ images are filtergrams; they unambiguously show where the emission occurs. The location where the emission is observed in the $\mathcal{I}_{-1}$ and $\mathcal{I}_{+1}$ images depends on the emission spectra. The dispersion direction in these images is in the horizontal (x, solar E–W) direction. Emission at 304 Å will image to the same location in all of the $\mathcal{I}_m$ (a result achieved through co-alignment during data preparation; see Section 3.1). Emission to the blue of 304 Å will be shifted to the left in $\mathcal{I}_{-1}$ and to the right in $\mathcal{I}_{+1}$. Emission to the red of 304 Å will be shifted to the right in $\mathcal{I}_{-1}$ and to the left in $\mathcal{I}_{+1}$.

The white crosshairs in the panels are approximately centered on the compact sources as observed in the $\mathcal{I}_0$ (middle row). The red and blue line segments, labeled $+100\,\mathrm{km\,s^{-1}}$ and $-100\,\mathrm{km\,s^{-1}}$, respectively, are displaced along the x (dispersion) axis from the white vertical line segment. These labeled lines represent the horizontal displacement expected in $\mathcal{I}_{-1}$ and

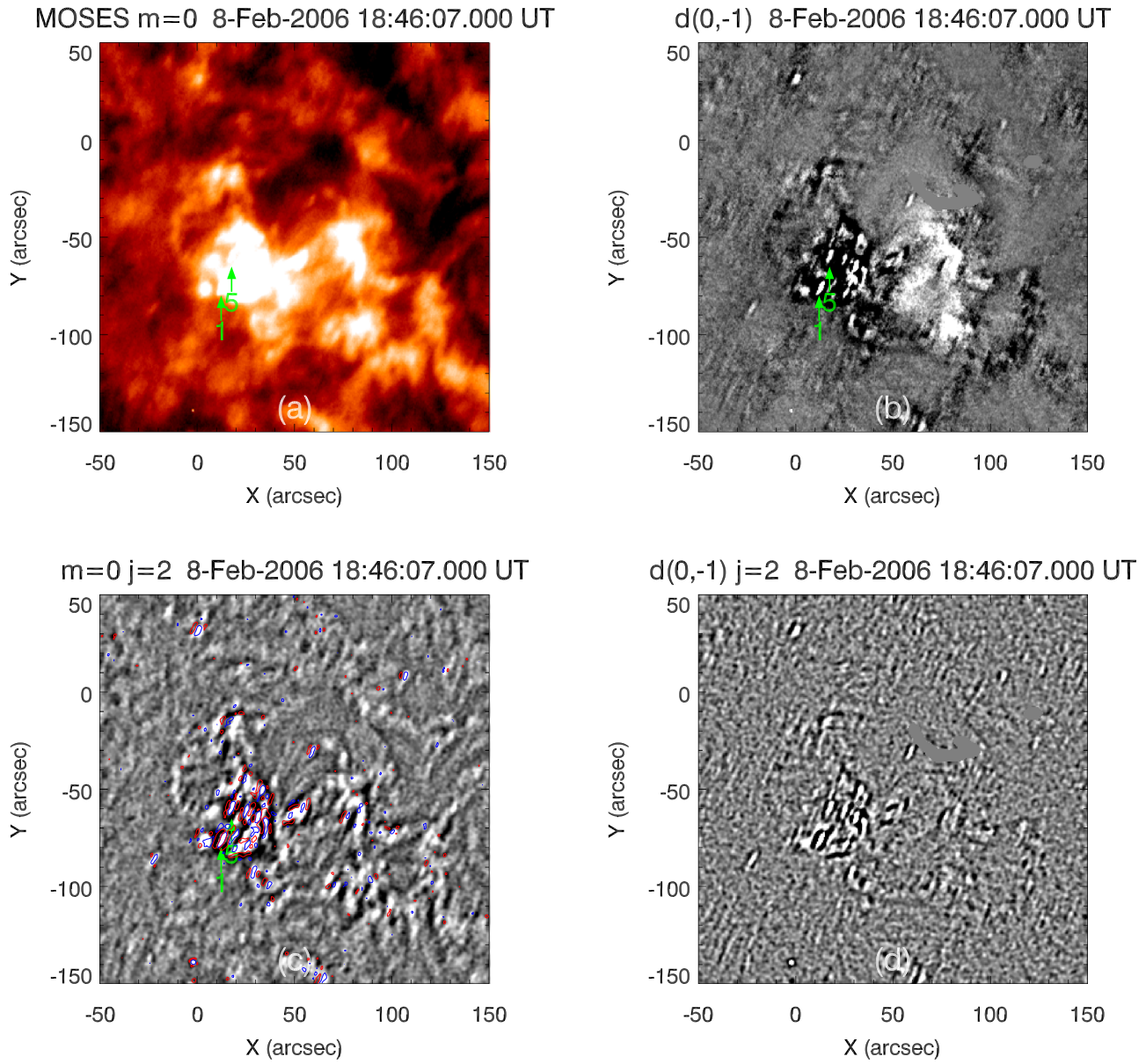

Figure 7. Close-up of a quiet-Sun region with relatively strong underlying magnetic network (NW box in Figure 2). Panels show (a) log-scaled $\mathcal{I}_0$ intensity, (b) difference image $d_{(0,-1)}$, (c) the $j = 2$ wavelet coefficients $\tilde{\mathcal{I}}^2_z$, and (d) the scale $j = 2$ wavelet coefficients $\tilde{d}^2_{(0,-1)}$. The 3σ contours of $\tilde{d}^2_{(0,-1)}$ are overplotted onto the $\tilde{\mathcal{I}}^2_z$ image. Blue contours are positive differences, and red contours are negative. Numbered arrows point to explosive events identified in this paper that are visible at the time shown in the figure. An animation of this figure is available in the online journal. The animation shows the full sequence of 27 observations over the ~5-minute flight. The animation makes it easy to see how explosive event candidates are found in the data as bright compact features in the difference and intensity images that appear to flicker, some transient, others lasting the duration of the flight. Explosive events identified in this paper are labeled with numbered arrows at times when they are clearly visible.

(An animation of this figure is available.)

$\mathcal{I}_{+1}$ given an emission source centered in x on the vertical white crosshair as observed in $\mathcal{I}_0$, emitting at 304 Å and moving with a line-of-sight velocity of $+100$ and $-100\,\mathrm{km\,s^{-1}}$, respectively (see Equation (2)). The magnitude of the shift, about 3.4 pixels, is determined by combining the linear dispersion of the spectrograph ($29\,\mathrm{m\,Å\,pixel^{-1}}$; see Table 2) and the Doppler relation $\Delta\lambda/\lambda = v/c$. The Doppler width of each pixel in the dispersed channels, $29\,\mathrm{km\,s^{-1}}$, is also shown in Table 2. These red, white, and blue line segments are used in several figures in this paper as fiducial markers to give scale to shifts observed in the dispersed images. A value of $100\,\mathrm{km\,s^{-1}}$ is used as a characteristic speed for explosive events.

In each column the $\mathcal{I}_0$ data show a roughly rectangular bright object with 5″ spatial extent centered in the white crosshairs. The objects in each of the separate $\mathcal{I}_0$ observations have a similar appearance to one another. As seen in $\mathcal{I}_{-1}$ and $\mathcal{I}_{+1}$, the left column (a) observation shows a compact object centered horizontally on the vertical white crosshair. The middle column (b) observation shows a compact object centered on the blue ($-100\,\mathrm{km\,s^{-1}}$) line in both $\mathcal{I}_{-1}$ and $\mathcal{I}_{+1}$. The right column (c)

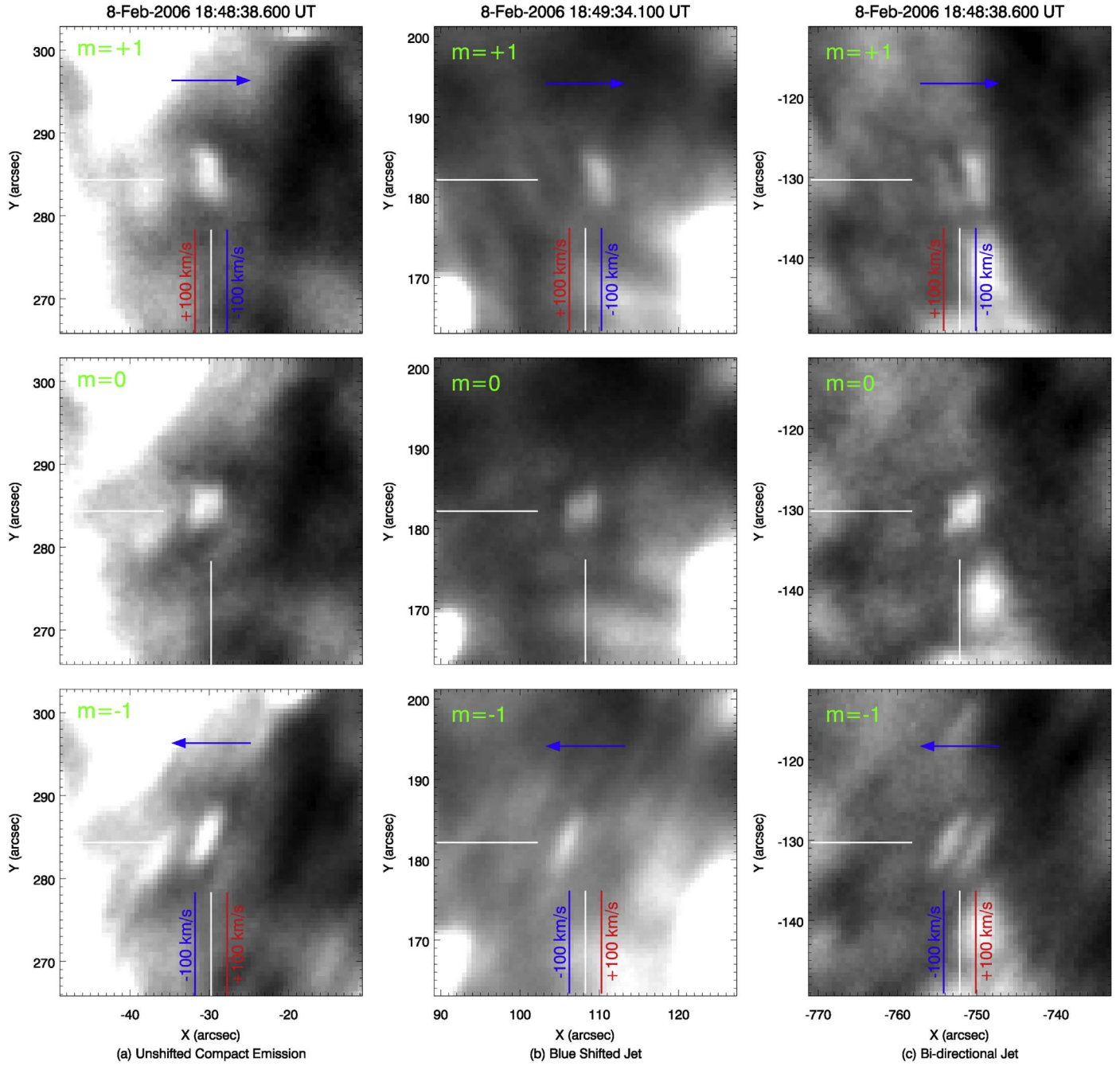

Figure 8. Snapshots of three compact objects, one per column, observed with *MOSES-06*. The fields of view for the observations in each column are shown in Figure 2. The panels in a given column show, from top to bottom, the $\mathcal{I}_{+1}$, $\mathcal{I}_0$, and $\mathcal{I}_{-1}$ data. The arrows indicate the blueshift direction in the dispersed orders. The object of interest in each column is a compact brightening near the center of each panel (white crosshairs). From left to right: (a) a compact source without significant Doppler shift; (b) a blueshifted jet—the compact emission seen in $\mathcal{I}_0$ has been shifted right in $\mathcal{I}_{+1}$ and left in $\mathcal{I}_{-1}$; (c) a bidirectional jet—the compact emission seen in $\mathcal{I}_0$ has been split into two components in $\mathcal{I}_{-1}$ and $\mathcal{I}_{+1}$, one component shifted to the right and one to the left relative to $\mathcal{I}_0$. The blue and red vertical line segments serve as fiducial marks and represent the horizontal displacement expected in $\mathcal{I}_{-1}$ and $\mathcal{I}_{+1}$ given a compact source centered on the vertical white crosshair as observed in $\mathcal{I}_0$, emitting at 304 Å, and moving with a line-of-sight velocity of -100 and $+100$ km s^{-1}. See Equation (2), Table 2, and the discussion in Section 5. This figure is available as an animation in the online journal. The animation shows the full sequence of observations of these three objects over the 5-minute duration of the *MOSES-06* flight. The objects, not visible at the start of the animation, brighten against the background emission at approximately (a) 18:47:15 UTC, (b) 18:49:34 UTC, and (c) 18:48:10 UTC. The abrupt brightening allows one to easily distinguish between the object and background emission. Co-temporal brightening in all three *MOSES-06* spectral orders leaves no doubt that the shifted/split components seen in the column (b) and (c) $\mathcal{I}_{-1}$ and $\mathcal{I}_{+1}$ observations are the same emission as that observed as a single compact brightening in $\mathcal{I}_0$.

(An animation of this figure is available.)

observation shows two components to the object seen in $\mathcal{I}_{-1}$ and $\mathcal{I}_{+1}$. One component is centered over the blue (-100 km s^{-1}) line, and one component is centered over the red ($+100$ km s^{-1}) line.

These observations each have simple interpretations. The top left column (a) observation is a compact source emitting at He II λ304. The middle column (b) observation is a blueshifted

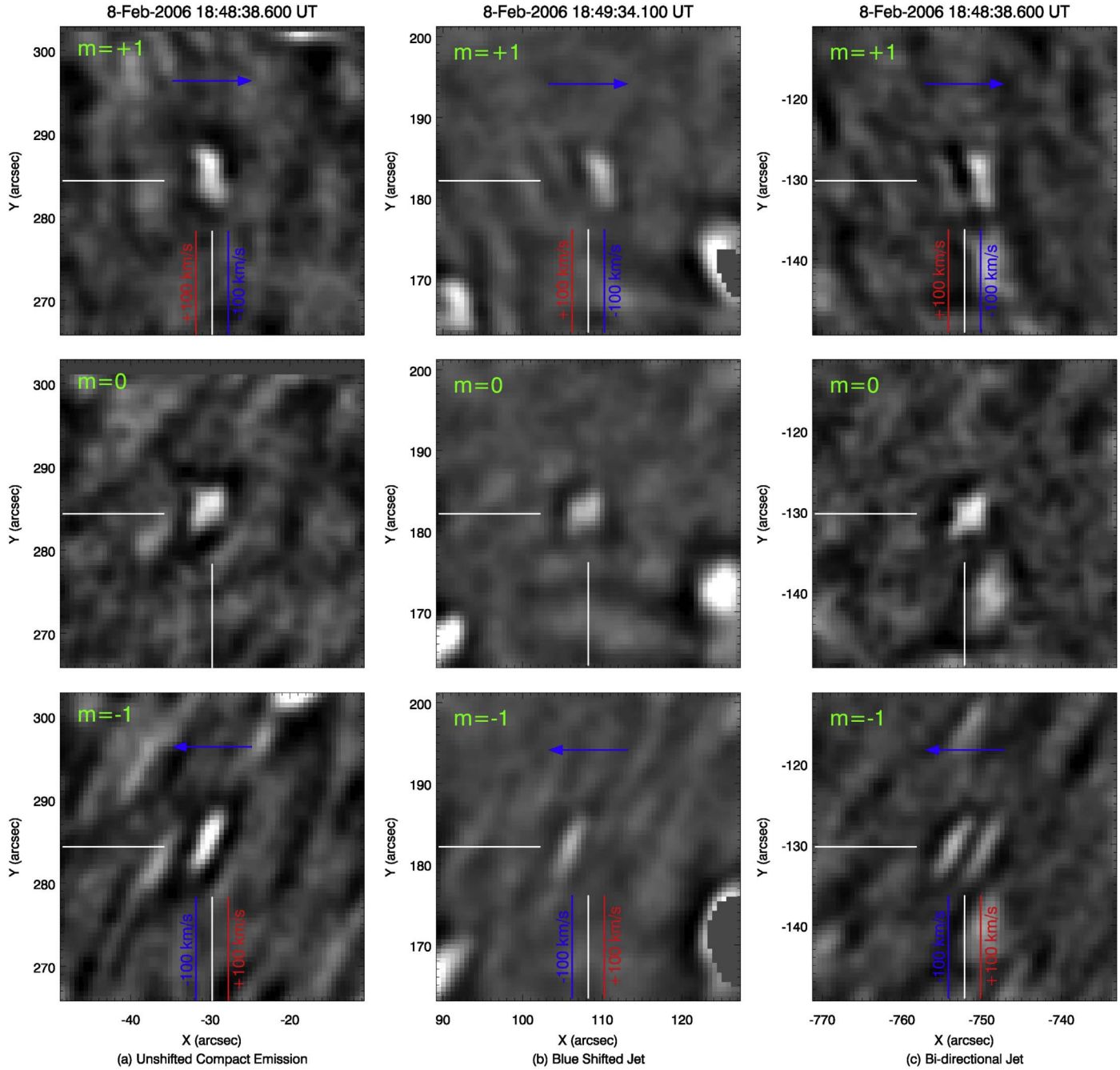

Figure 9. Scale $j = 2$ wavelet coefficients of the compact objects of Figure 8. See Figure 8 for a description of the figure panels and annotations. Empirically the $j = 2$ coefficients best show the structure in these objects while filtering out high-frequency noise and low spatial frequency background emission. The visual contrast of the objects of interest with respect to the background is markedly improved relative to the intensity data of Figure 8. This figure is available as an animation in the online journal. The animation shows the $j = 2$ wavelet coefficients of the full sequence of observations of these three objects over the duration of the *MOSES-06* flight. Given the increased contrast in the wavelet data, the objects can be clearly distinguished somewhat earlier than in the image data, at approximately (a) 18:46:44 UTC, (b) 18:49:24 UTC, and (c) 18:48:01 UTC. As with the image data of Figure 8, the animation makes it very easy to visually distinguish the explosive event from other emission in the field of view, as the compact emission brightens abruptly in all three spectral orders.

(An animation of this figure is available.)

($-100\,\mathrm{km\,s^{-1}}$) He II λ304 jet, and the right column (c) observation is a bidirectional ($\pm 100\,\mathrm{km\,s^{-1}}$) He II λ304 jet.

Figure 9 shows the scale $j = 2$ wavelet coefficients of the observations from Figure 8. These wavelet images show the small-scale structure in the observations. The $j = 2$ coefficients were chosen because they seem to best show the object structure. The $j = 1$ (smallest-scale) coefficients are very noisy. The $j = 3$ coefficients appear blurred, e.g., the prominent gap between the two jet components in column (c) observations is smoothed out in the $j = 3$ coefficients.

The small-scale structure of the observations is highlighted in the $j = 2$ wavelet coefficients because high-contrast but slowly varying background emission has been filtered out of the data. While the different objects show different spectral characteristics as described above, there are also similarities between the different observations. It has already been noted

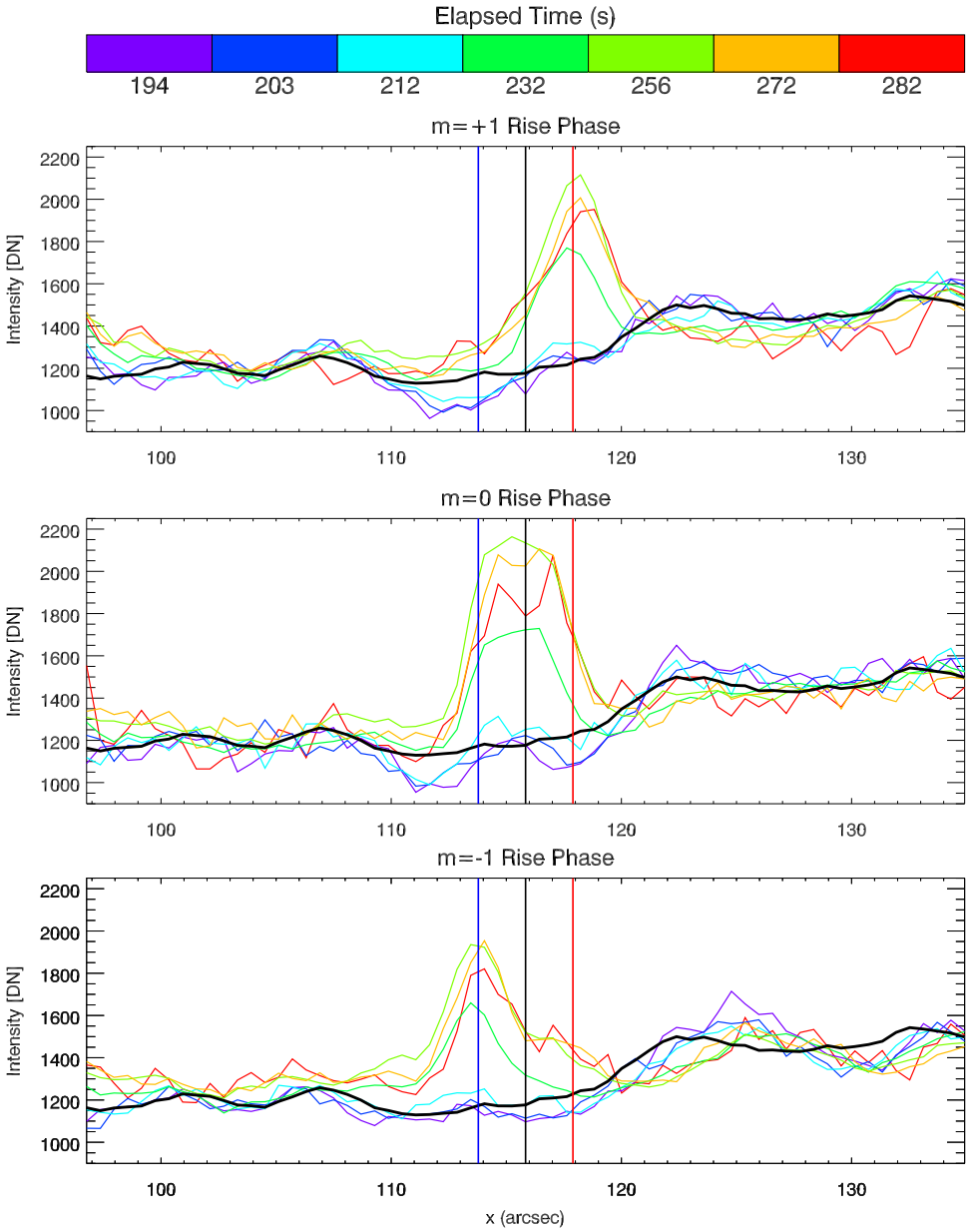

Figure 10. Rise phase of the blueshifted jet. Profiles are taken along the horizontal white lines in the panels of Figure 8. From top to bottom the plots show the $\mathcal{I}_{+1}$, $\mathcal{I}_0$, and $\mathcal{I}_{-1}$ profiles. Elapsed times are from the beginning of the *MOSES-06* data sequence to the middle of a given exposure. Fiducial lines in the images mark the locations of -100 km s^{-1} (blue line) and $+100$ km s^{-1} (red line) Doppler shifts relative to the black line. The thick black curve is an approximate background level; see text for details.

that the shape of each object is similar in the $\mathcal{I}_0$ channel. In the $\mathcal{I}_{-1}$ and $\mathcal{I}_{+1}$ channels, the shapes of the shifted emission in the blue jet (column (b), Figures 8 and 9) are similar to the shapes of the unshifted emission in the column (a) observation: a SE to NW trending slash in $\mathcal{I}_{-1}$ and a SW to NE trending slash in $\mathcal{I}_{+1}$. The bidirectional jet (column (c), Figures 8 and 9) as seen in $\mathcal{I}_{-1}$ and $\mathcal{I}_{+1}$ has two shifted components. The shapes of each of these components are themselves very similar to the shapes of the shifted and unshifted components in the column (a) and (b) observations. Many more examples of these shapes associated with compact sources emission in the *MOSES-06* data are shown in Rust (2017, Appendix D). It is most likely that this common spatial structure seen in compact emission is due to the instrument point-spread functions. The *MOSES-06* primary mirror is a square aperture off-axis sphere, and the design is therefore astigmatic. Combined astigmatism and defocus can largely explain the observed shape of the point-spread functions.

The point-like object is not the only emission present in the observations. A complicated intensity distribution constitutes a background to the object of interest in each of the $\mathcal{I}_m$. Movies of these objects (Figures 8 and 9 animations in online journal) clearly support a distinction between the compact objects and the background. The compact objects brighten suddenly without noticeable change in the surrounding background intensity. Significantly, the background intensity distribution is approximately the same in each of the $\mathcal{I}_m$. This can be seen clearly in the upper right panel difference image in Figure 6. The strong difference region at $[-750'', -130'']$ corresponds to the bidirectional jet observation (column (c), Figure 8) and is confined to the neighborhood of the compact emission seen in the $\mathcal{I}_0$ channel. Surrounding the strong difference region, the

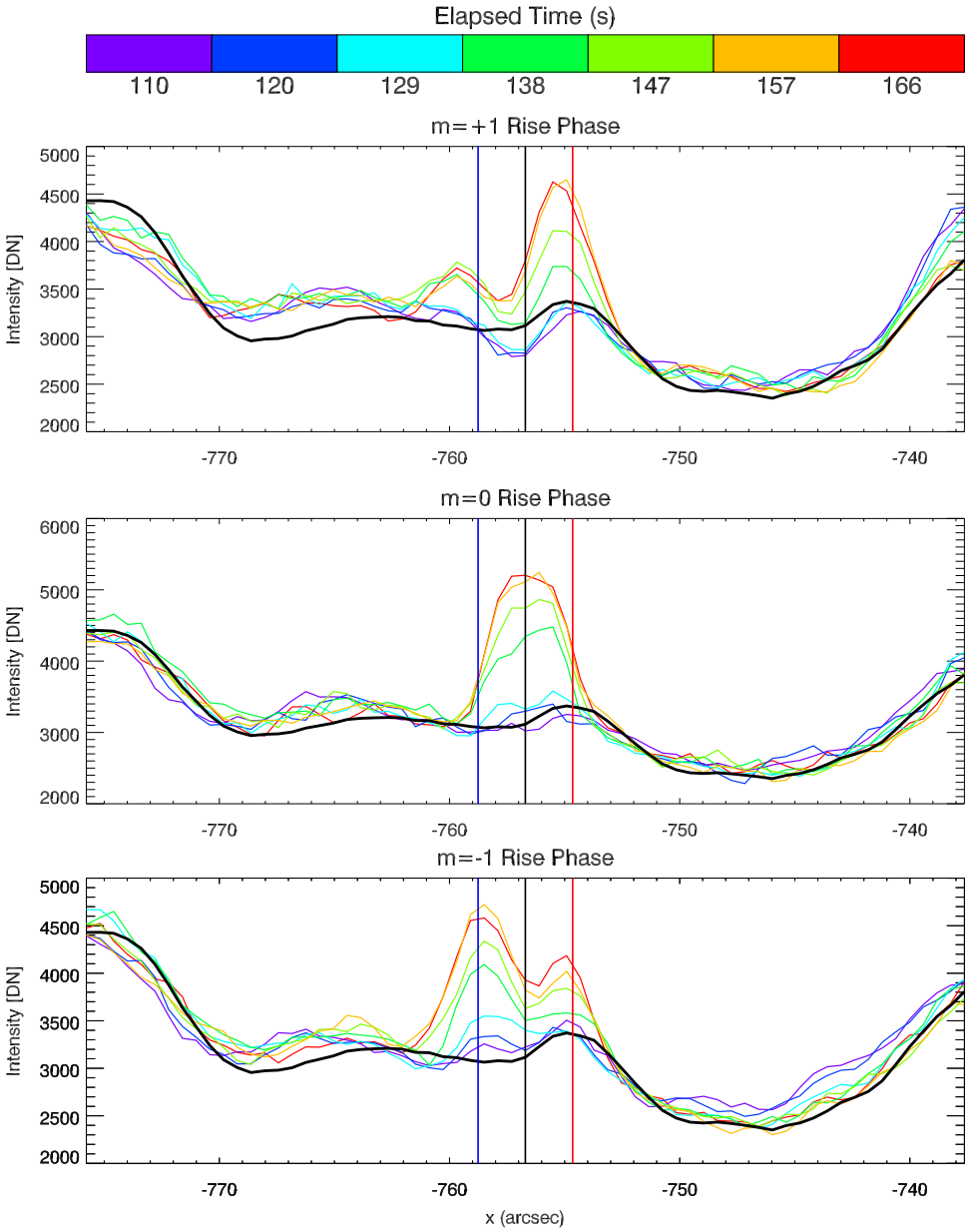

Figure 11. Rise phase of the bidirectional jet. See caption of Figure 10 and the text for details.

gray scale indicates weak differences, e.g., the $\mathcal{I}_m$ have approximately equal intensity in this wider region. One possible explanation for this background is spatial variation in the intensity of a spatially uniform He II λ304 line profile, e.g., the quiet-Sun profile measure by Andretta et al. (2000).

Regardless of the exact nature of the background, there is a clear distinction between the compact source and the background. This can be seen in the line plots in Figures 10 and 11, which show the rise phase of the blue jet and bidirectional jet, respectively. The profiles are E–W profiles (i.e., along the dispersion direction) through the centers of the compact objects as seen in the $\mathcal{I}_0$. The panels in Figures 10 and 11 show, from top to bottom, the $\mathcal{I}_{+1}$ profiles, the $\mathcal{I}_0$ profiles, and the $\mathcal{I}_{-1}$ profiles. The thicker black profile shown in each panel is the average of a number of profiles from earlier in the flight. The average is taken over time (multiple exposures) and over spectral order (i.e., averaged over $\mathcal{I}_{-1}$, $\mathcal{I}_0$, and $\mathcal{I}_{+1}$). This average profile represents an approximation to the background on which the explosive events are seen to rise. As in Section 5, the vertical blue and red lines indicate the expected shifts (relative to the vertical black line) due to line-of-sight velocities of $\pm 100\,\mathrm{km\,s^{-1}}$. The times given are elapsed time (s) since 18:45:54 UT in the middle of a given exposure.

5.1. Blue Jet Rise Phase

The rise phase of the blue jet is shown in Figure 10. The blue jet rise phase shows a "switch-on" character within the time resolution of the *MOSES-06* observations. The three profiles in each spectral order at $t = 194$ s, $t = 203$ s, and $t = 212$ s vary little with time and track reasonably well with the black background profile. Seen in $\mathcal{I}_0$ (middle panel), the compact source is first clearly present at $t = 232$ s, brightens further by $t = 256$ s, and then appears to fade slightly at $t = 272$ s and again at $t = 282$ s. The profile at $t = 282$ s is from a short (1.5 s) exposure and is somewhat underexposed and noisy. The

$\mathcal{I}_0$ profiles of the blue jet appear to change in amplitude but not in shape or location. The vertical black lines in the panels of Figure 10 indicate the approximate position of the center of the brightening observed in the $\mathcal{I}_0$.

The top and bottom panels of Figure 10 show the $\mathcal{I}_{+1}$ and $\mathcal{I}_{-1}$ profiles of the blue jet. These profiles also show a "switch-on" character. Through $t = 212$ s the profiles track with the background profile, and then at $t = 232$ s brightening occurs. The vertical blue and red vertical lines plotted over the $\mathcal{I}_{-1}$ and $\mathcal{I}_{+1}$ profiles indicate the expected shifts (relative to the vertical black line) due to $\pm 100\,\mathrm{km\,s^{-1}}$ Doppler speeds. The brightening in the $\mathcal{I}_{-1}$ and $\mathcal{I}_{+1}$ profiles at $t = 232$ s is approximately centered on the blue vertical line. The profiles brighten further at $t = 256$ s and then get slightly dimmer at later times. As with the $\mathcal{I}_0$ profiles, the evolution of the $\mathcal{I}_{-1}$ and $\mathcal{I}_{+1}$ profiles predominantly suggests amplitude changes of a fixed profile shape. Over the observation period the peak of the brightening seen in $\mathcal{I}_{-1}$ and $\mathcal{I}_0$ remains approximately centered at $100\,\mathrm{km\,s^{-1}}$ blueshift (the blue vertical line).

The observed rise phase of the jet seen in $\mathcal{I}_{-1}$ and $\mathcal{I}_{+1}$ will depend on the acceleration and heating of the emitting plasma, where the term "heating" refers to the process that leads to enhanced emission in the He II λ304 line within the jetting region. If the heating precedes the acceleration, there should be brightening at small shifts in $\mathcal{I}_{-1}$ and $\mathcal{I}_{+1}$, which is not observed. If heating occurs during acceleration, then the rise phase profiles in $\mathcal{I}_{-1}$ and $\mathcal{I}_{+1}$ should brighten at a range of Doppler speeds, with the detailed profile depending on the plasma acceleration and heating, as well as the temporal and spectral resolution of the observations. The profile at $t = 232$ s is a 24 s exposure preceded by 6 s of readout time. Sometime over this 30 s period the jet brightens, and 24 s of evolution are integrated to form the $t = 232$ s profiles. These profiles are broad, but much of that broadening is attributable to the point-spread functions. Most of the emission is from fast-moving ($-100\,\mathrm{km\,s^{-1}}$) plasma. This implies that either the heating trails the plasma acceleration or the acceleration up to about $-100\,\mathrm{km\,s^{-1}}$ is very rapid. After reaching $-100\,\mathrm{km\,s^{-1}}$, the plasma speed remains approximately constant for at least the next 50 s.

The profiles and movies (Figures 8 and 9 animations in online journal) of this object show hints that there is also a redshifted component to this event. In the profiles this is seen as a broad shoulder on the red side of the vertical black line, which rises starting at $t = 256$ s. In the movie it is fairly clear that there is a faint red component. The blueshifted emission clearly dominates, however, hence the characterization of this object as a blueshifted jet.

5.2. Bidirectional Jet Rise Phase

The rise phase intensity profiles of the bidirectional jet are shown in Figure 11. The cadence of these observations (about 10 s) is more rapid than the cadence during the blue jet rise phase. The $\mathcal{I}_0$ profiles (middle panel of Figure 11) show a gradual brightening starting at $t = 129$ s and continuing until $t = 157$ s, with roughly half of the peak brightness reached by $t = 138$ s. The profile is approximately unchanged in the next exposure at $t = 166$ s. This brightening again appears to be an amplitude change of a particular profile shape, which is almost certainly the profile of the point-spread function $\mathcal{P}_0$.

As the jet brightens in $\mathcal{I}_0$, it also brightens in $\mathcal{I}_{+1}$ and $\mathcal{I}_{-1}$ (top and bottom panels of Figure 11, respectively). At the earliest stage of the brightening ($t = 129$ s) the $\mathcal{I}_{-1}$ and $\mathcal{I}_{+1}$ profiles are indistinct. The most significant deviation of these profiles from the background profile (black line) at this time is the peak just to the red of the $-100\,\mathrm{km\,s^{-1}}$ indicator (blue vertical line) in the $\mathcal{I}_{-1}$ profile. By $t = 138$ s a two-component profile is plainly visible in both $\mathcal{I}_{-1}$ and $\mathcal{I}_{+1}$. The blue and red components in the $\mathcal{I}_{-1}$ profiles peak at about $\pm 90\,\mathrm{km\,s^{-1}}$ as seen in the plotted profiles. The blue and red components in the $\mathcal{I}_{+1}$ profiles suggest about -75 and $+150\,\mathrm{km\,s^{-1}}$, respectively.

The blue component in both the $\mathcal{I}_{-1}$ and $\mathcal{I}_{+1}$ profiles brightens in a similar fashion to the brightening in the $\mathcal{I}_0$ profiles, reaching peak brightness over the period shown at $t = 157$ s and then maintaining that profile in the next exposure at $t = 166$ s. The locations of the blue peaks do not change significantly during the rise phase. Curiously, the red component in $\mathcal{I}_{-1}$ appears to brighten throughout the rise phase, while the red component in the $\mathcal{I}_{+1}$ profiles reaches peak brightness by about $t = 138$ s and then maintains that amplitude. In the movies (Figures 8 and 9 animations in online journal) there appears to be a faint secondary brightening seen in the $\mathcal{I}_0$ images to the NW of the jet center. This secondary source may contribute to the discrepancies between the $\mathcal{I}_{-1}$ and $\mathcal{I}_{+1}$ observations with respect to the red component evolution and the observed shift magnitudes.

The evolution of the profiles during the bidirectional jet rise phase has a similar character to the blue jet: brightening of a fixed profile shape. This shows as well in the movies. At no time do the $\mathcal{I}_{-1}$ and $\mathcal{I}_{+1}$ profiles appear to be dominated by emission from low-speed plasma. After brightening, the shifted peak locations do not change significantly; the plasma appears to reach a preferred speed and then remain there. If the plasma is emitting during acceleration, the 10 s cadence of these observations places an upper bound on the time required for the plasma to reach this preferred speed, i.e., significantly less than 10 s. Otherwise, emission from low-speed plasma during acceleration would blur the $\mathcal{I}_{-1}$ and $\mathcal{I}_{+1}$ profiles, and more emission would be present at small shifts. At the observed temporal resolution there is a pronounced gap between the blue and red components of the $\mathcal{I}_{-1}$ and $\mathcal{I}_{+1}$ profiles when they first brighten ($t = 138$ s), which indicates that not much emission is present from low-speed plasma. Alternatively, it is possible that the heating lags the acceleration in time.

The full time evolution of both the blueshifted jet and the bidirectional jet is shown in columns (b) and (c) of Figure 12. These figures show stack plots of dispersion direction intensity profiles through the centers of the jets. The unshifted compact source (column (a) of Figure 8) is also shown in column (a) of Figure 12 for comparison. The red and blue lines overplotted on the stack plots again show the expected $\pm 100\,\mathrm{km\,s^{-1}}$ shift locations relative to the overplotted white lines. The first and final two *MOSES-06* exposures have been excluded from Figure 12 because they are very noisy. The blue jet is present in four exposures lasting approximately 60 s. The bidirectional jet is present in 13 exposures lasting 145 s. These lifetimes are lower bounds, and the events may last beyond the end of the *MOSES-06* flight.

5.3. Doppler Shift Estimates

The analysis thus far has relied on image fiducial marks for visual estimation of the speeds of Doppler-shifted components observed in a blueshifted jet and a bidirectional jet. In this

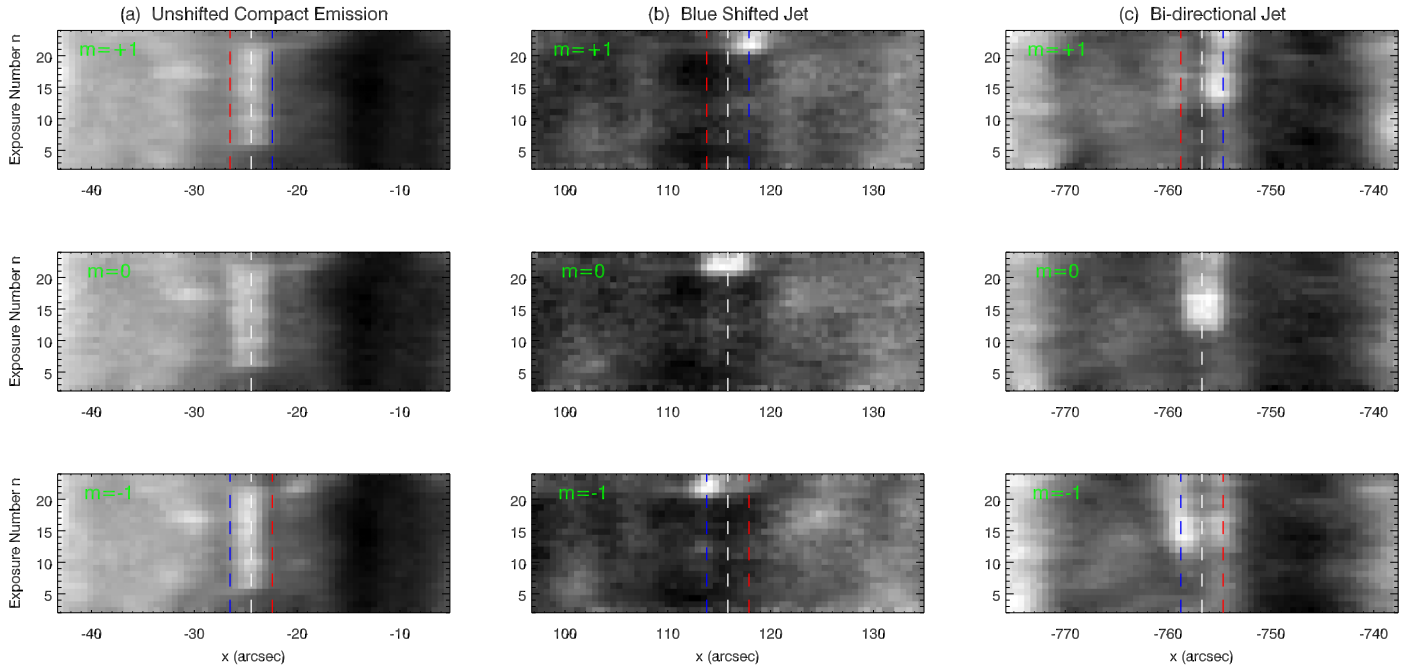

Figure 12. Stack plots of profiles through the compact objects of Figure 8 with position on the horizontal axes and time (as exposure number) on the vertical axes. Fiducial lines in the images mark the locations of -100 km s^{-1} (blue line) and $+100$ km s^{-1} (red line) Doppler shifts relative to the white vertical line. The columns from left to right show (a) the unshifted compact emission, (b) the blueshifted jet, and (c) the bidirectional jet. Within each column the panels show the $\mathcal{I}_{+1}$, $\mathcal{I}_0$, and $\mathcal{I}_{-1}$ profiles from top to bottom. The stack plots show profiles from exposure $n = 2$ to exposure $n = 24$. The remaining exposures are fairly noisy.

section estimates of the numerical values of these speeds will be made by fitting the intensity profiles with one Gaussian component (blueshifted jet) and two Gaussian components (bidirectional jet). This type of fitting to obtain velocity estimates from *MOSES-06* data is similar to the "parallax analysis" of Fox et al. (2010). Detailed line profile estimates from tomographic inversion will be addressed in an upcoming paper (in preparation).

It has been discussed in Section 5 how the compact objects of Figure 8 appear in $\mathcal{I}_0$ as essentially copies of the instrument point-spread functions. To within the *MOSES-06* resolution, then, these objects are effectively point-like. As was further discussed, the objects appear to rise out of background emission, which does not significantly vary between the $\mathcal{I}_m$. Following a suitable background subtraction, therefore, these objects are essentially isolated point objects. Given the shift magnitudes, the brightness of these sources, and the fact that the *MOSES-06* passband is dominated by He II λ304 (Fox 2011, and references therein), it is reasonable to assume that the emission is dominated by this single spectral line. As per the discussion in Section 1.3.1, the $\mathcal{I}_{-1}$ and $\mathcal{I}_{+1}$ dispersion direction spatial profiles through these objects are expected to be mirrored about object centers and proportional to the spectral line profiles of the underlying point sources. The line profiles may be described directly as a function of Doppler shift.

Figures 13 and 14 show the $\mathcal{I}_{-1}$, $\mathcal{I}_0$, and $\mathcal{I}_{+1}$ profiles of the blue jet and bidirectional jet, respectively, after subtracting off the black background profile shown in Figures 10 and 11. The blue jet profile is taken from exposure number $n = 22$. The bidirectional jet profile is from $n = 15$. The profile in each spectral order is fitted with one or two Gaussians as appropriate. The velocity scale is set by the $\mathcal{I}_0$ profile fit, with zero velocity corresponding to the centroid of the $\mathcal{I}_0$ fit.

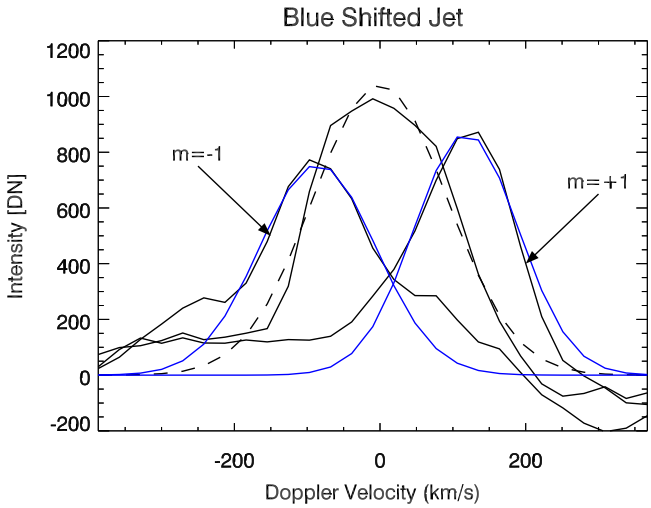

Figure 13. Blue jet Doppler shift estimates made by single Gaussian fitting to background-subtracted dispersion direction $\mathcal{I}_{-1}$ and $\mathcal{I}_{+1}$ profiles through the explosive event. The conversion from position to Doppler velocity on the horizontal axis is described in Sections 1.3.1 and 5.3. Zero velocity is set by the centroid of a Gaussian fit to the $\mathcal{I}_0$ profile. Mean jet velocity is estimated as the centroid of the Gaussian fits to the $\mathcal{I}_{-1}$ and $\mathcal{I}_{+1}$ profiles and is shown in Table 4.

The fits (Figure 13) to the blue jet components are best in the component cores near the peak intensity. The fits remain good over a span of about 150 km s^{-1} (about the width of the point-spread functions), which covers most of the emission. The fit centroids then should be a good approximation to the Doppler velocity of the blueshifted emission.

The fits (Figure 14) to the bidirectional jet components show good agreement with the data in two important respects. First, the fits well describe the peak regions of the jet components and thus should provide accurate Doppler shift estimates.

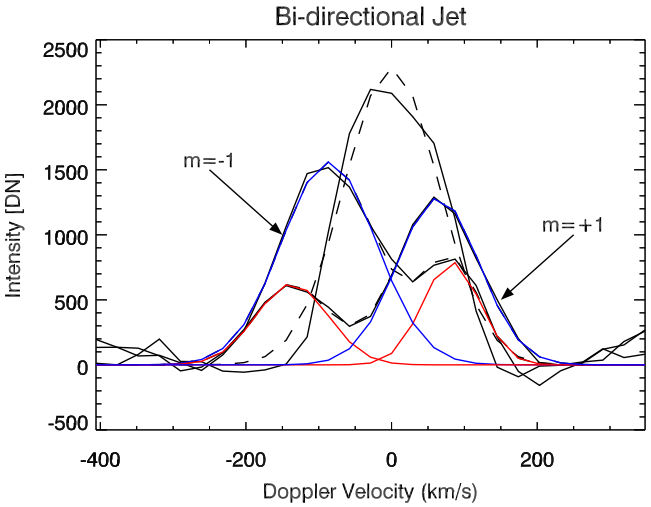

Figure 14. Bidirectional jet Doppler shift estimates made by two-Gaussian fitting to background-subtracted dispersion direction $\mathcal{I}_{-1}$ and $\mathcal{I}_{+1}$ profiles through the explosive event. The red component fit is shown in red, the blue component fit in blue. The conversion from position to Doppler velocity on the horizontal axis is described in Sections 1.3.1 and 5.3. Zero velocity is set by the centroid of a Gaussian fit to the $\mathcal{I}_0$ profile. Mean jet component velocities are estimated from the centroids of the two-Gaussian fits to the $\mathcal{I}_{-1}$ and $\mathcal{I}_{+1}$ profiles and are shown in Table 4.

Second, note how well the two-component model fits the $\mathcal{I}_{-1}$ and $\mathcal{I}_{+1}$ profiles at small Doppler velocities where the components overlap. This is a clue that the emission seen at low velocities is probably due to limited instrument resolution rather than actual emitting plasma.

The estimated Doppler speeds for the blue jet and bidirectional jet are summarized in Table 4.

5.4. Magnetic Context

The speeds of the Doppler-shifted components in the above examples are an order of magnitude larger than the expected width of the thermal velocity distribution at the He II λ304 formation temperature. This indicates that the energy driving the plasma flows is probably magnetic energy transferred to the plasma during magnetic reconnection. The magnetic contexts of the blue jet and bidirectional jet (red crosses) are shown in the top and bottom rows of Figure 15.

The blue jet location sits along an arc of locally strong positive-polarity magnetic concentrations. These may be network fields in the downflow lane between supergranular cells. The diameter of the arc is about 20″, which is a reasonable diameter for a supergranule cell. The bidirectional jet is found next to the weaker of a pair of positive-polarity magnetic concentrations. The surrounding region is characterized by weak mixed-polarity fields.

Magnetic reconnection models predict a characteristic speed for plasma outflows along reconnecting field lines. This speed is the Alfvén speed v_A:

$$v_A = \frac{B}{\sqrt{4\pi\rho}}, \tag{5}$$

where $\rho = n_e m_p$ is the plasma density, n_e is the electron density, m_p is the proton mass, and B is the magnetic field strength. Assuming a pressure $P = 0.05\,\mathrm{dyne\,cm^{-2}}$ and temperature $T = 80{,}000\,\mathrm{K}$ (MacPherson & Jordan 1999), $n_e = 2.3 \times 10^9\,\mathrm{cm^{-3}}$ and $\rho = 3.8 \times 10^{-15}\,\mathrm{g\,cm^{-3}}$. The extent to which the emitting plasma traces reconnecting field lines depends on the plasma $\beta = 8\pi P/B^2$, the ratio of the gas and magnetic pressures. When $\beta \ll 1$, the plasma is frozen onto the field lines. Figure 16 shows β and v_A plotted as a function of the magnetic field strength.

Table 4
Jet Speeds ($\mathrm{km\,s^{-1}}$) Derived from Gaussian Fits

	Blue Jet	BD Jet Red	BD Jet Blue
$m = -1$	−85	+82	−86
$m = +1$	−118	+136	−64

The magnetic field strengths present in the blue and bidirectional jet examples are estimated from a potential field extrapolation of the photospheric magnetic field to be 9 and 7 G, respectively. The calculated plasma β is then 0.015 in the blue jet and 0.025 in the bidirectional jet. In both cases β is small, and thus the emission should trace reconnecting field lines. Assuming that the density derived above is appropriate for the reconnection region, the expected Alfvén speeds are about $400\,\mathrm{km\,s^{-1}}$ for the blue jet and $300\,\mathrm{km\,s^{-1}}$ for the bidirectional jet. These values are in excess of what is observed by a factor of four (see Table 4). The plasma density was calculated using an assumed filling factor—the ratio of observed volume to emitting volume—of unity. Dere et al. (1987) found filling factors of 1% in observations of C IV λ1548 in the transition region. An independent density measurement would help to constrain the expected Alfvén speed.

5.5. Mass and Kinetic Energy Flux

The spectral signatures of the blue jet and the blue component of the bidirectional jet suggest a flow of mass and energy from the reconnection site upward into the atmosphere. The total mass in the upward flow is approximated as

$$M = \rho A v t, \tag{6}$$

where ρ is the density derived above, A is the cross-sectional area of the outflow, v is the outflow speed, and t is the event lifetime. The total kinetic energy carried by the flow is

$$E_K = \frac{1}{2} M v^2. \tag{7}$$

The minimum lifetime for the blue jet is $t_{\mathrm{blue}} = 60\,\mathrm{s}$. The minimum lifetime of the bidirectional jet is $t_{\mathrm{bd}} = 145\,\mathrm{s}$. The area of the outflow region can be approximated from the area of the brightening seen in these events in the $\mathcal{I}_0$ channel. These areas are approximately 5″ wide, but given the size of the *MOSES-06* point-spread functions, the true outflow area must be much smaller than this. Assuming a circular outflow area of diameter 1″ gives $A = 2.1 \times 10^{16}\,\mathrm{cm^2}$. The average upward outflow speeds in the blue jet and bidirectional jet are 101 and $75\,\mathrm{km\,s^{-1}}$, respectively (see Table 4). Using these parameters, the total mass and kinetic energy flow upward from the reconnection sites is given in Table 5 assuming a filling factor of 1. The kinetic energy values are within the range given by Winebarger et al. (2002).

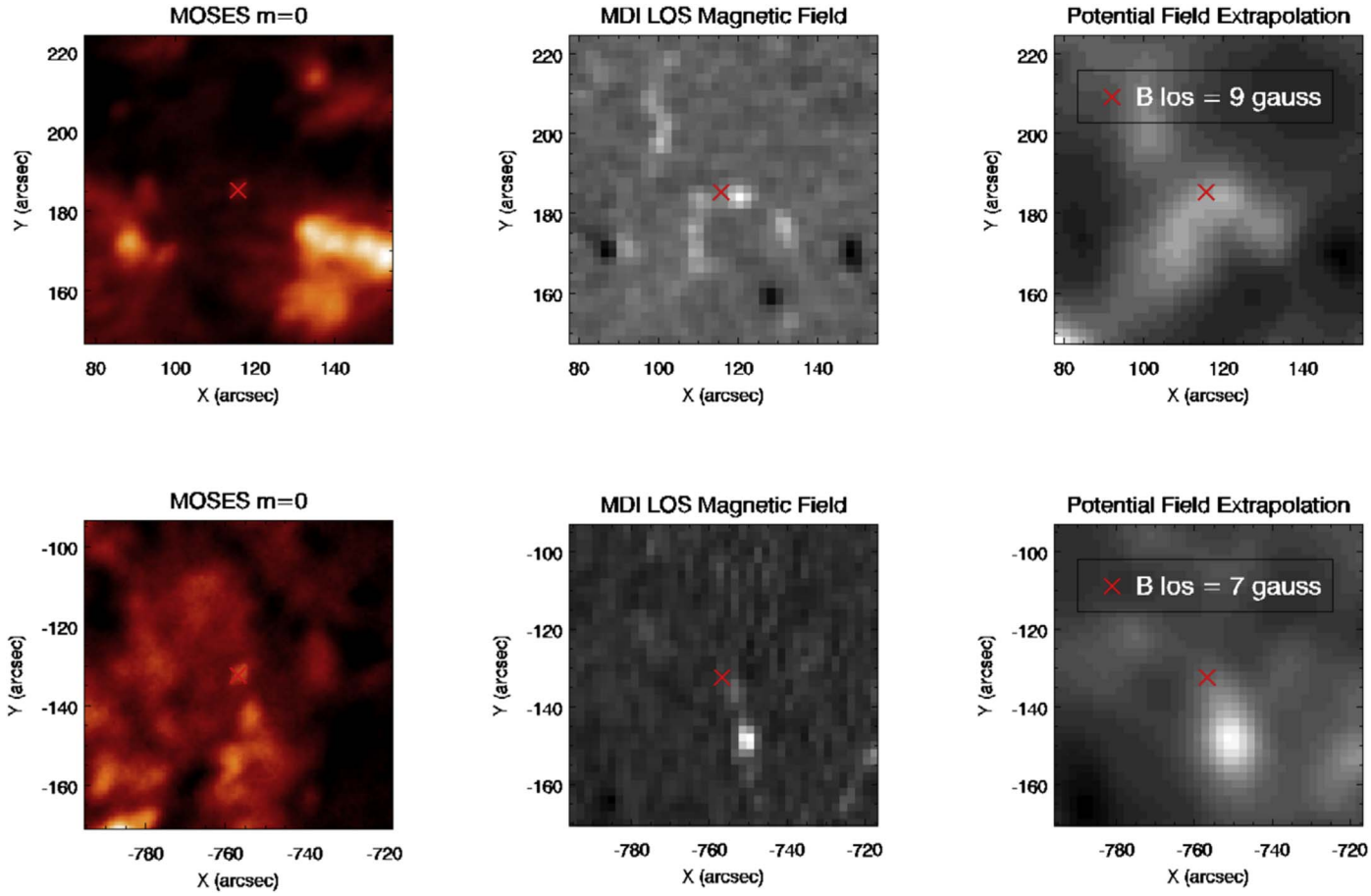

Figure 15. Magnetic context of the blue jet (top) and bidirectional jet (bottom). Panels from left to right show intensity (log scaled), MDI photospheric line-of-sight magnetic field strength, and potential field extrapolation up to 5750 km above the photosphere. Jet locations are marked with a red cross. (Field extrapolation provided by Dr. Dana Longcope.)

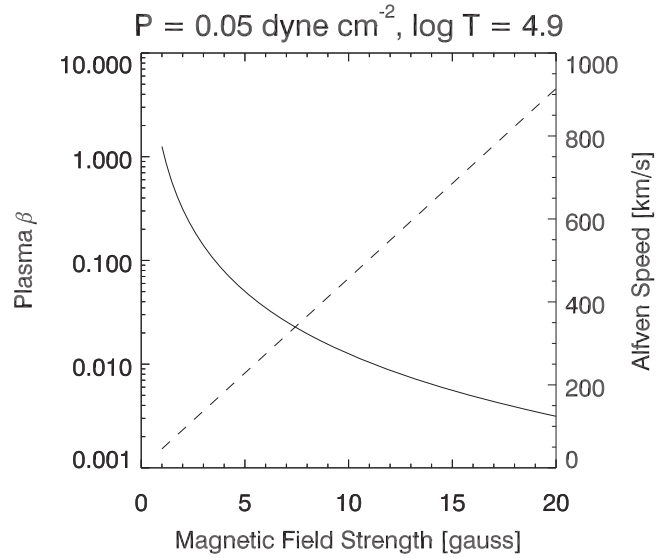

Figure 16. Plasma β (solid) and the Alfvén speed (dashed) in the transition region.

6. Additional Explosive Event Examples

The events in this section were selected manually based on clear evidence of strong Doppler shifts in the *MOSES-06* image data. Candidate locations were selected based on strong difference image signatures; many candidates were rejected because the differences appeared to be artifacts due to the point-spread functions (see Section 4 for further discussion about identification of explosive events in *MOSES-06* data). The locations of identified explosive events are plotted on $\mathcal{I}_0$ in Figure 2. A close-up view of the coronal hole is shown in Figure 5. The objects themselves are shown in Figure 17. Panels 1 through 41 are snapshots of different explosive events. Panels 42 through 45 are examples of compact emission without obvious shifts and are included to show the shape of the point-spread functions. The panels are arranged into three subpanels with the $\mathcal{I}_{-1}$, $\mathcal{I}_0$, and $\mathcal{I}_{+1}$ data from bottom to top. The events are displayed as the scale $j = 2$ wavelet coefficients in order to show the small-scale structure. The strong influence of the instrument point-spread functions can be seen in all of these observations.

Table 5
Estimates for the Upward Mass and Kinetic Energy Flow from the Blue Jet and Bidirectional Jet

Jet	M (g)	E_K (erg)
Blue jet	9.5×10^9	4.8×10^{23}
Bidirectional jet	1.7×10^{10}	4.8×10^{23}

The explosive events were classified as red jets, blue jets, or bidirectional jets if the $\mathcal{I}_m$ visually supported that designation. Red jet examples are shown in Figure 17, panels 10 and 35.

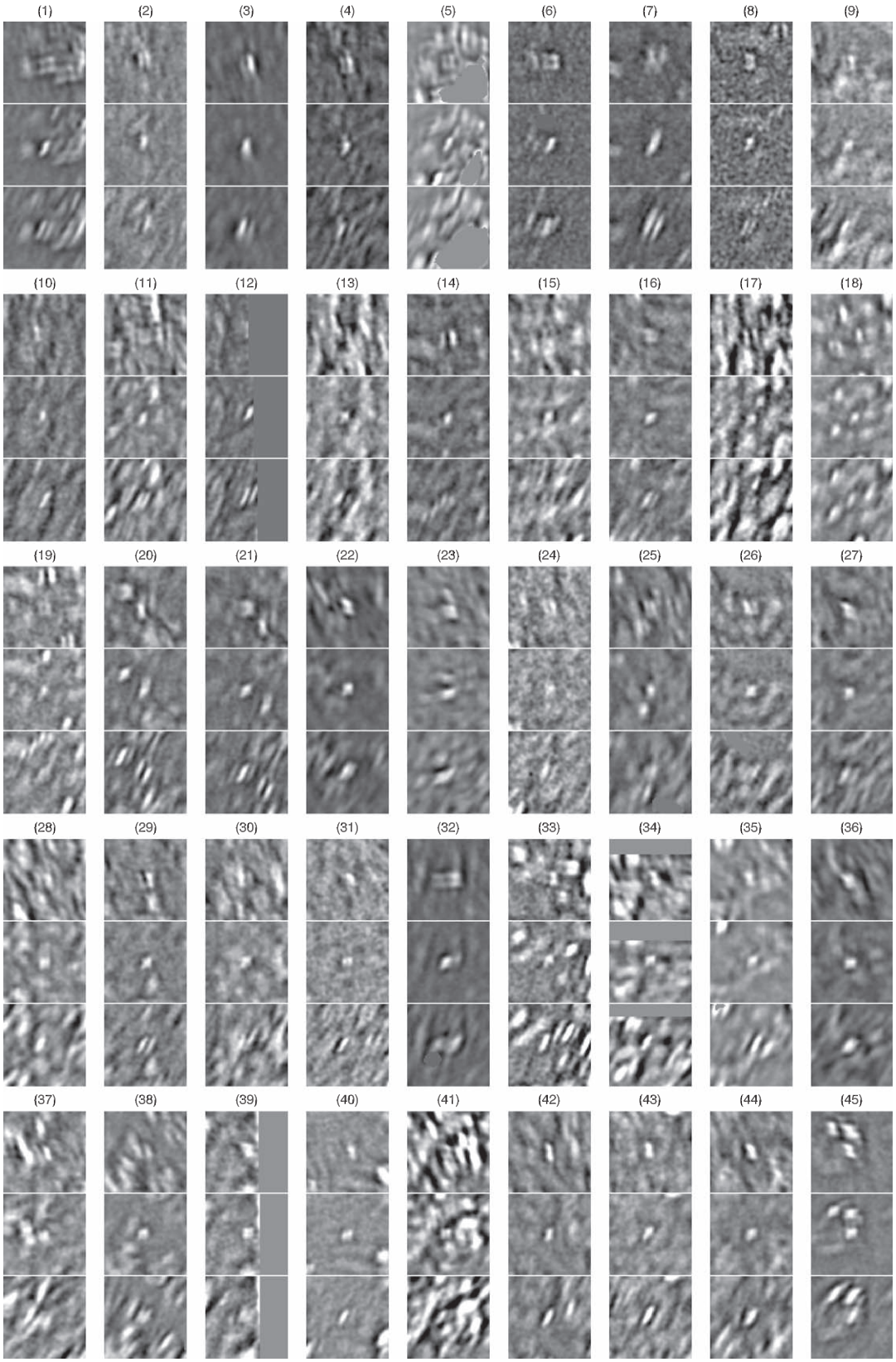

Figure 17. Panels 1–41 show examples of explosive events observed by *MOSES-06*, presented here as the scale $j = 2$ wavelet coefficients of the $\mathcal{I}_m$. Each panel has three subpanels. Subpanels from top to bottom: $\mathcal{I}_{+1}$, $\mathcal{I}_0$, and $\mathcal{I}_{-1}$. Each subpanel has a $37\farcs5$ field of view. In each example a compact, isolated bright patch is seen in the center of the middle subpanel ($\mathcal{I}_0$). The top and bottom subpanels ($\mathcal{I}_{+1}$, $\mathcal{I}_{-1}$) of the explosive events show some combination of shifting, splitting, or broadening of the emitting region. Panels 42–45 show examples of compact objects that are not explosive events. The morphologies of these objects are dominated by the instrument point-spread functions, and these same shapes—back slash in top subpanel, stretched rectangle in middle subpanel, and forward slash in bottom subpanel—may be seen in all of the explosive event examples. Uniform gray areas are missing data.

Table 6
Properties of Explosive Events Observed with *MOSES-06*

Property	No. Occurrences	Magnetic Properties	Value
Red jet	2 (5%)	No. events	34
Blue jet	5 (12%)	$\langle \lvert B \rvert \rangle$	8.0 G
Bidirectional jet	10 (24%)	$B_{\rm min}$	−19 G
Bidirectional jet*	8 (20%)	$B_{\rm max}$	61 G
Other	16 (39%)	No. $B > 0$	28 (82%)
Coronal hole	12 (29%)	No. $B < 0$	4 (12%)
Quiet Sun	28 (68%)	No. $B = 0$	2 (6%)

Note. The left table summarizes the event types and locations; the right table summarizes the event magnetic properties. Bidirectional jet* indicates that the event appears strongly bidirectional in one of the $\mathcal{I}_{-1}$ or $\mathcal{I}_{+1}$ but not the other. *B* values are from the potential field extrapolation. Seven of the 41 explosive events fall outside the field extrapolation field of view, so only 34 events are characterized magnetically. See text for further description.

Blue jet examples are shown in Figure 17, panels 18, 31, 33, 34, and 40. Bidirectional jet examples are shown in Figure 17, panels 1, 3, 7, 15, 17, 20, 24, 26, 29, and 32. Events classified as bidirectional jet* are events that appear strongly bidirectional in one of the $\mathcal{I}_{-1}$ or $\mathcal{I}_{+1}$ but not the other. Examples of bidirectional jet* are shown in Figure 17, panels 5, 8, 11, 12, 16, 19, 27, and 28. The remaining events, classified as other, are for one reason or another difficult to classify in the previous categories. In all, 12 events out of 41 (29% of all events) were identified within the coronal hole, which is only about 5% of the *MOSES-06* field of view. These results are summarized in the left-hand table of Figure 6.

Figure 3(d) shows the explosive event locations plotted over the MDI magnetogram. The overplotted contours are the +5 G (white) and −5 G (black) contours of a potential field extrapolation provided by Dr. Dana Longcope. The field was extrapolated from the MDI photospheric magnetic field measurements to a height of about 5750 km above the photosphere within a field of view of $x \in [-799'', 198'']$ and $y \in [-302'', 300'']$. The explosive event locations are overplotted with a green dot at each event site. The MDI data have been derotated by 2 hr to account for the time difference between the magnetic and *MOSES-06* measurements.

The magnetic contexts of 34 out of 41 total explosive events are characterized on the right side of Table 6. Seven events were not included because they fell outside of the field of view of the magnetic field extrapolation. More than 80% of 34 events were found in positive field regions. The mean field magnitude averaged over all events is 8.0 G, although examples exist within regions of stronger field. Two explosive events are found in regions with no measurable line-of-sight magnetic field. Inspection of Figure 3(d) shows that many events are located near the boundary where weak mixed field regions meet unipolar field concentrations. Of the 34 events within the extrapolation field of view, 24 (70.5%) are located within 10″ of a 5 G contour line.

7. Summary

This paper describes *MOSES-06* observations of He II λ304 emission in the solar transition region. Of particular interest, many compact, bright features in the images have been identified as transition region explosive events. The spatial structure of the compact features is heavily influenced by the point-spread functions, different in each image channel.

The rise and time evolutions of two example events, a blueshifted jet and a bidirectional jet, were examined in detail. The Doppler speeds associated with the jet components were calculated by assuming that the intensity distribution in the *MOSES-06* dispersed channels was equivalent to the average spectrum of the event plus a variable background. Upon background subtraction and Gaussian fitting the example events show Doppler speeds of approximately 75–100 km s^{-1}.

Characteristic of both types of jets is an apparent lack of emission from low-speed plasma. The blue jet line profile can be described with a single Gaussian component that peaks at a Doppler velocity of approximately 100 km s^{-1} (Figure 13). The bidirectional jet line profile can be described by two Gaussian components with peak shifts of −75 and +100 km s^{-1} (Figure 14). The bidirectional jet components are well separated, and the two-Gaussian fit well describes the low-velocity region of the line profile, suggesting that the observed low-velocity emission may be due to the instrument resolution. Regardless of the precise strength of the low-velocity emission, the example event line profiles are dominated by high-speed emission.

It is interesting to contrast these observations with the explosive events observed in Si IV λ1402 with *IRIS* by Innes et al. (2015). The Si IV line profiles have significant emission at high velocity but are dominated by a low-velocity core. The line profiles may sometimes be well represented by a single broad Gaussian (Innes et al. 2015). As the Si IV line profiles evolve in time, they sometimes show additional brightening at low velocity, which Innes et al. (2015) argue is evidence for tearing mode reconnection based on magnetohydrodynamic (MHD) modeling. The example *MOSES-06* explosive events have weak line core emission and show no indication of core brightening over the observation period. The bidirectional jet in particular supports the Petschek reconnection explosive event model of Innes & Tóth (1999) rather than the tearing mode model of Innes et al. (2015). The difference between the He II and Si IV line profiles—core dominated versus wing dominated—may indicate that He II and Si IV explosive events fall in different regions of the reconnection phase diagram of Ji & Daughton (2011). It would be interesting to investigate the relationship between He II and Si IV explosive events via a *MOSES* underflight of *IRIS*.

The MHD model of Innes et al. (2015) also predicts an acceleration phase at the onset of an explosive event, wherein emitting plasma is accelerated to the Alfvén speed. Detailed examination of the rise phase of the two example explosive events shows no indication of an early acceleration phase. Both the blue and bidirectional jets had a "switch-on" characteristic where from first appearance the event line profiles are wing dominated. See the discussion in Sections 5.1 and 5.2.

In total, 41 explosive events from the *MOSES-06* data were identified and have been classified according to their location and event type. Almost 30% of the identified events were located in a coronal hole in the NW corner of the *MOSES-06* field of view. The coronal hole covers just 5% of the field of view. The coronal hole lacks network emission, and the He II λ304 intensity distribution is somewhat simpler than in the quiet Sun. It is possible that a selection bias exists that favors coronal hole explosive events in the *MOSES-06* data. However, experience suggests that the coronal hole has an unusual density of explosive events relative to the surrounding quiet Sun as observed with *MOSES-06*. In order to develop the tentative conclusion that He II λ304 explosive events occur

preferentially in coronal holes, it will be necessary to carefully evaluate selection biases in the identification of explosive events. Automatic detection of explosive events and evaluation of selection bias is a major goal of future work.

Line-of-sight magnetic field data from *SOHO*-MDI were used to provide magnetic context for the *MOSES-06* observations. A potential field extrapolation was employed to estimate magnetic field strength in the transition region at explosive event sites. The average magnetic field strength over all identified explosive events is 8 G. At this field strength the Alfvén speed is of order 100 km^{-1} given a reasonable estimate for the transition region density.

The authors wish to thank Dr. Dana Longcope for helping to analyze and interpret the magnetic observations and Dr. Piet Martens and Dr. Jim Klimchuk for helpful discussions about the physical properties of explosive events and the transition region.

References

Andretta, V., Jordan, S. D., Brosius, J. W., et al. 2000, ApJ, 535, 438
Brueckner, G. E., & Bartoe, J.-D. F. 1983, ApJ, 272, 329
Cargill, P. 2013, A&G, 54, 3.16
Chae, J., Wang, H., Lee, C.-Y., Goode, P. R., & Schühle, U. 1998, ApJL, 497, L109
Delaboudinière, J. P., Artzner, G. E., Brunaud, J., et al. 1995, SoPh, 162, 291
DePontieu, B., Title, A. M., Lemen, J. R., et al. 2014, SoPh, 289, 2733
Dere, K. P., Bartoe, J.-D. F., & Brueckner, G. E. 1984, ApJ, 281, 870
Dere, K. P., Bartoe, J.-D. F., & Brueckner, G. E. 1989, SoPh, 123, 41
Dere, K. P., Bartoe, J.-D. F., Brueckner, G. E., Cook, J. W., & Socker, D. G. 1987, SoPh, 114, 223
Dere, K. P., Bartoe, J.-D. F., Brueckner, G. E., Ewing, J., & Lund, P. 1991, JGR, 96, 9399
Fox, J. L. 2011, PhD thesis, Montana State Univ.
Fox, J. L., Kankelborg, C. C., & Thomas, R. J. 2010, ApJ, 719, 1132
Freeland, S., & Handy, B. 1998, SoPh, 182, 497
Holschneider, M., Kronland-Martinet, R., Morlet, J., & Tchamitchian, P. 1990, in Wavelets. Time-Frequency Methods and Phase Space, ed. J.-M. Combes, A. Grossmann, & P. Tchamitchian (Berlin: Springer), 286
Innes, D. E. 2001, A&A, 378, 1067
Innes, D. E., Guo, L.-J., Huang, Y.-M., & Bhattacharjee, A. 2015, ApJ, 813, 86
Innes, D. E., Inhester, B., Axford, W. I., & Wilhelm, K. 1997, Natur, 386, 811
Innes, D. E., & Tóth, G. 1999, SoPh, 185, 127
Ji, H., & Daughton, W. 2011, PhPl, 18, 111207
Jordan, C. 1975, MNRAS, 170, 429
Kak, A. C., & Slaney, M. 1988, Principles of Computerized Tomographic Imaging (New York: IEEE Press), http://www.slaney.org/pct/pct-toc.html
Kankelborg, C. C., & Thomas, R. J. 2001, Proc. SPIE, 4498, 16
MacPherson, K. P., & Jordan, C. 1999, MNRAS, 308, 510
Ning, Z., Innes, D. E., & Solanki, S. K. 2004, A&A, 419, 1141
Owens, S. M., Gum, J. S., Tarrio, C., et al. 2005, Proc. SPIE, 5900, 5
Parker, E. N. 1988, ApJ, 330, 474
Petschek, H. E. 1964, NASSP, 50, 425
Porter, J. G., & Dere, K. P. 1991, ApJ, 370, 775
Priest, E., & Forbes, T. 2007, Magnetic Reconnection (Cambridge: Cambridge Univ. Press)
Rust, T. L. 2017, PhD thesis, Montana State Univ.
Savage, S. L., McKenzie, D. E., & Reeves, K. K. 2012, ApJL, 747, L40
Scherrer, P. H., Bogart, R. S., Bush, R. I., et al. 1995, SoPh, 162, 129
Shensa, M. J. 1992, ITSP, 40, 2464
Teriaca, L., Banerjee, D., Falchi, A., Doyle, J. G., & Madjarska, M. S. 2004, A&A, 427, 1065
Tousey, R., Bartoe, J. D. F., Bohlin, J. D., et al. 1973, SoPh, 33, 265
Wilhelm, K., Curdt, W., Marsch, E., et al. 1995, SoPh, 162, 189
Winebarger, A. R., Emslie, A. G., Mariska, J. T., & Warren, H. P. 2002, ApJ, 565, 1298
Withbroe, G. L., & Noyes, R. W. 1977, ARA&A, 15, 363